The Dissertation Committee for Sahar Elahi Certifies that this is the approved version of the following dissertation:

IVOCT Imaging Artifacts of Coronary Stents

Committee:

Thomas E. Milner, Supervisor

Marc D. Feldman, Co-Supervisor

Jouke Dijkstra

Andrew K. Dunn

James W. Tunnell

Aaron B. Baker

IVOCT Imaging Artifacts of Coronary Stents

by

Sahar Elahi, B.MED.E.; M.S.

Dissertation

Presented to the Faculty of the Graduate School of

The University of Texas at Austin

in Partial Fulfillment

of the Requirements

for the Degree of

Doctor of Philosophy

The University of Texas at Austin

August 2013

Dedication

To my dear parents Dr. Homayoun Elahi and Dr. Saeideh Mozafari

who could not have been more supportive.

Acknowledgements

I would like to express my sincere gratitude to my supervisor Dr. Thomas Milner for his continuous support throughout my PhD study. Dr. Milner has been a true mentor as well as an inspiration, without his guidance this work would not have been possible.

I am grateful to Dr. Marc Feldman for assistance with clinical aspects and Dr. Jouke Dijkstra for many helpful discussions.

I would like to thank my fellow researchers Dr. Jordan Dwelle, Dr. Tianyi Wang, Austin McElroy, Biwei Yin, Derek Ho and Derek Hernandez.

I would like to express my deepest love and appreciation to my parents for their unconditional love and support. They have always believed in me and could not have done more to help me achieve my dreams. They have been an inspiration for me and I hope this will make them proud.

Finally, I would like to thank my cute little dog Pasha who never failed to put a smile on my face! :)

IVOCT Imaging Artifacts of Coronary Stents

Sahar Elahi, Ph.D.

The University of Texas at Austin, 2013

Supervisor: Thomas E. Milner

Co-Supervisor: Marc D. Feldman

Coronary stent placement is a routine treatment of coronary artery disease, the leading cause of death worldwide. Intravascular Optical Coherence Tomography (IVOCT) is a superior imaging assessment technique in coronary stenting. To characterize IVOCT artifacts, phantom blood vessels were constructed and metallic and bioabsorable coronary stents were deployed with and without phantom neointima. High resolution Micro-CT images of the stent strut were recorded as a gold standard and utilized to create a three-dimensional representation of a strut that was imported into computer optical simulations. Simulated IVOCT images were computed that include the IVOCT catheter, light reflection from stent struts with varying neointimal thickness and scattering in the vessel lumen. The simulation results along with IVOCT images of the phantom vessels were utilized to elucidate the mechanisms underlying the "sunflower effect", bending of stent struts toward the imaging catheter and "merry-go-round" effect, variable apparent strut size of metallic stents. Atomic force microscopy was used to examine surface properties of metallic and bioabsorbale stents, revealing sources of the distinctive appearance of bioabsorable stents in IVOCT images. The model formed a basis to develop a correction algorithm to remove stent artifacts in clinical IVOCT images.

Table of Contents

List of Tables

List of Figures

Chapter 1: Introduction

The objective of my research is to characterize and correct artifacts that arise when imaging stents in coronary arteries with intravascular optical coherence tomography (IVOCT). In 2008, coronary artery disease (CAD) caused almost 1 of every 6 deaths in the United States. Over the next two decades, projected costs for all cardiovascular diseases are expected to increase 61% with CAD accounting for almost 40% [1]. Three types of stents for CAD have been introduced over the last two decades: these include 1) bare metal stents; 2) drug eluting stents; and 3) bio-absorbable stents. After stent deployment, assessment of stent apposition and tissue growth over struts requires diagnostic imaging. Although intravascular ultrasound (IVUS) has been utilized to assist with stenting coronary arteries, resolution (80-120 um) is limited. In comparison to IVUS, IVOCT provides higher image resolution by one order of magnitude (10-15 um) making this technique a preferred assessment technique in coronary stenting of coronary arteries. Clinical use of IVOCT to assess coronary stenting will benefit from the characterization and correction of various artifacts. Specific aims of my research include:

- Describing the underlying mechanism of sunflower artifact - bending of stent struts towards the catheter at eccentric positions in the vessel lumen
- Presenting an accurate and verified method of strut apposition measurement
- Evaluation of IVOCT in neointima thickness measurement
- investigate merry-go-round effect - elongation of the stent struts - due to residual blood not completely removed by flushing and neointimal coverage over the stent
- Identifying the mechanism(s) for differences in IVOCT images of bioabsorbable vs. metallic stents

- Developing an artifact correction algorithm for metallic stents which replaces the apparent stent struts rendered in IVOCT images recorded during a pullback with the actual stent structure obtained by Micro-CT imaging.

ORGANIZATION OF THE DISSERTATION

Chapter 2 "Coronary artery disease: diagnostics and treatments" provides an overview to coronary artery disease and coronary stents. A brief history of advancements in different stent types, as well as imaging modalities utilized during stent deployment are presented. Principles of IVOCT imaging and its applications in stenting are discussed. Lastly, imaging artifacts associated with IVOCT images are introduced which motivates this work.

Chapter 3 "Models for studying IVOCT artifacts" describes the two models that were created; a physical blood vessel model and a computer model. Construction of phantom vessels and stent deployment are included, followed by description of Micro-CT and IVOCT imaging protocols. Computer model was created by defining an IVOCT catheter and importing a strut model in ZEMAX, non-sequential ray tracing was performed and ray data was imported to MATLAB for analysis.

Chapter 4 "IVOCT measurement of size and apposition of metallic stents" begins with investigating the factors contributing to variation in apparent size of struts in IVOCT images. Sunflower effect is reproduced in IVOCT images of phantom vessels and simulated images in the computer model which is utilized to ellucidate the origin of this artifact. Knowing the actual position and orientation of struts in the models, an accurate method of malapposition measurement is proposed.

Chapter 5 "IVOCT imaging of coronary artery metallic stents with neointimal coverage" explores neonitimas in IVOCT images. Fabrication of phantom neointima which

covers the stents deployed within phantom vessels is described. IVOCT and Micro-CT images of phantom vessels with neointima are utilized to evaluate acuracy of IVOCT in neonitima thickness measurement. Effect of luminal scattering on detection of thin neonitma is examined. Additionally, merry-go-round and sunflower effects in presence of thick neointima are examined.

Chapter 6 “Bioabsorbable stents” explores the current status of bioabsorbable stent development. IVOCT and Micro-CT images of bioabsorbable stents are used to describe the appearance of stent struts. To compare bioabsorbable and metallic stents, surface optical properties are determined using atomic force microscopy and measurement of refractive index.

Chapter 7 “Metal stent artifact correction algorithm” describes developing an algorithm which replaces the apparent stent struts in IVOCT pullback images with the actual stent structure obtained by Micro-CT imaging. Creating stent database from Micro-CT images is described which formed the global coordinate system. A helix function is generated inside the stent which represents the position and direction of A-scans and is modified by catheter position and orientation. Stent positions that are recorded by the helix in local coordinate system form simulated pullback and is transformed into global coordinates using stent position and orientation. Simulated pullback and transformation parameters form an objective function that is utilized by Levenberg-Marquardt algorithm to fit to the IVOCT pullback data.

Chpater 8 “Conclusions and discussions” summarizes the results of this work and outlines future studies.

Chapter 2: Coronary artery disease: diagnostics and treatments

CORONARY ARTERY DISEASE

Coronary artery disease (CAD), also called coronary heart disease, is a leading cause of death in United States. Statistics of 2005-2008 show that 16.3 million people have CAD, about 8.3% of males and 6.1% of females [1]. CAD resulted in 405,309 deaths in 2008, accounting for approximately 1 of every 6 deaths in the United States. Costs for all cardiovascular diseases are projected to increase 61% (from $171.7 billion to $275.8 billion) between 2010 and 2030 and CAD is estimated to account for approximately 40% of total costs [1].

CAD is the atherosclerosis of the coronary arteries in which plaque builds up within the walls of the arteries that delivers oxygen to the myocardium and consist of blood-borne inflammatory and immune cells, vascular endothelial and smooth-muscle cells, lipids, and debris [2]. The presence of plaque buildup results in the narrowing of the arterial lumen - called stenosis - and the restriction of blood flow. Over time, reduction of oxygen-rich blood weakens the myocardium, however; the sudden rupture of these vulnerable plaques are the cause of heart attacks.

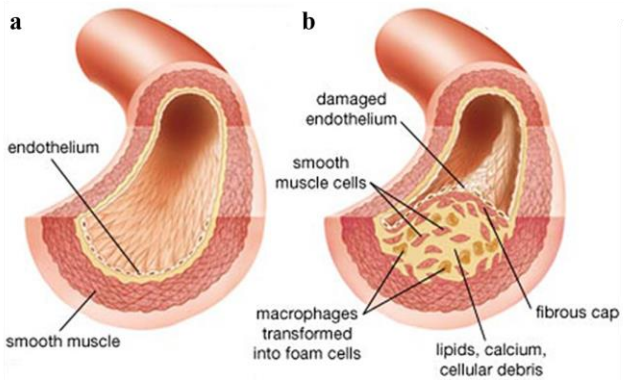

Figure 2.1: a) healthy coronary artery, **b)** stenotic coronary artery [3]

Treatment for CAD usually involves lifestyle changes, medications or medical procedures [4]:

- Lifestyle changes include: quitting smoking, eating healthy foods, a regular exercise routine, weight loss, stress reduction.
- Medications may slow the disease's progress or ease the symptoms and include cholesterol-lowering medications to decrease the primary material that deposits in the lumen of coronary arteries, blood thinners to reduce blood clotting capability, beta-blockers to decrease blood pressure.
- Bypass surgery: coronary artery bypass grafting is a heart procedure in which a section of a healthy blood vessel is connected (grafted) to coronary artery slightly past the site of the blockage to create a new path for blood to flow around (bypass) the blockage in the artery.
- Percutaneous coronary intervention (PCI): minimally invasive treatments to restore and improve blood flow, including:
    - Coronary balloon angioplasty: a balloon pushes back plaque and widens the artery, enabling blood to flow at a normal rate.
    - Stenting: a stent is an expandable, mesh-like cylindrical structure which provides structural support to maintain the artery open, allowing normal blood flow to the myocardium

STENT ADVANCEMENT

The first bare metal stent, Johnson & Johnson Palmaz-Schatz Balloon-Expandable Stent was introduced in the United States in 1994 [5]. While bare metal stents have been successfully used in treatment of CAD, some limitations associated with this technique have been identified, one of which is restenosis. After stent deployment, new tissue grows

inside the stent, developing a tissue lining over the stent which allows a smooth blood flow over the stented area. Later, however; the body's inflammatory response results in scar tissue formation underneath the new lining, which in about 25% of patients, obstructs the blood flow and produces an important blockage [6]. This condition, called in-stent restenosis, is typically seen 3 to 6 months after the stent deployment procedure [6]. Prevention of in-stent restenosis is achieved by a new generation of "drug-eluting" stents. Endeavor® Zotarolimus-Eluting Coronary Stent System was the first drug eluting stent approved by FDA in 2008 [7]. The surface of these metallic stents is covered by a polymer which releases immunosuppressant pharmaceuticals such as Sirolimus and paclitaxel over time to reduce scar tissue growth and prevent restenosis. Despite the widespread use of drug-eluting stents, there remains the issue of implantation of a permanent metallic intravascular prosthesis and the long-term body reaction. Stents composed of bioabsorbable materials represent an alternative modality which meets the short-term need for vessel scaffolding and avoidance of the potential long-term complications of metallic stents [8]. While the IGAKI-TAMAI stent, Kyoto Medical Planning Co., Ltd. obtained CE mark approval in 2007, bioabsorbable stents are still under clinical trial studies in the US required for FDA approval [9].

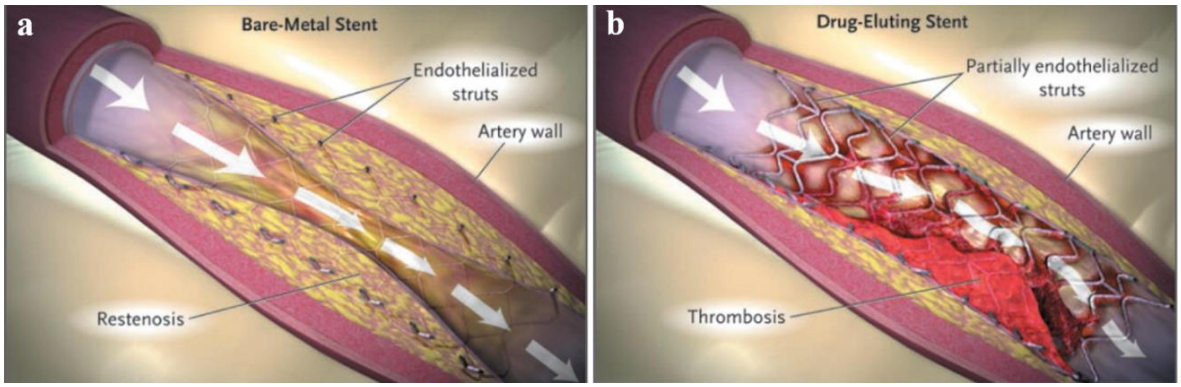

Figure 2.2: a) restenosis in BMS, **b)** Thrombosis in DES [10]

STENT DEPLOYMENT PROCEDURE

Stent deployment is performed in a catheterization clinic. Angiography is first utilized to assess the location and estimate the extent of the blockage and afterwards, IVUS is used to determine the luminal area of stenosis for stent sizing. Stents are packaged from the manufacturer in collapsed form, placed around a balloon at the tip of a catheter. Catheter is inserted through a small surgical opening in a blood vessel in the groin and guided to the stenotic artery. After positioning the still collapsed stent adjacent to the plaque region, balloon is inflated to a specified pressure which in turn expands the stent to a certain size. Balloon is deflated and removed along with the catheter, leaving the stent pressing against the plaque to keep the artery open and restore normal blood flow.

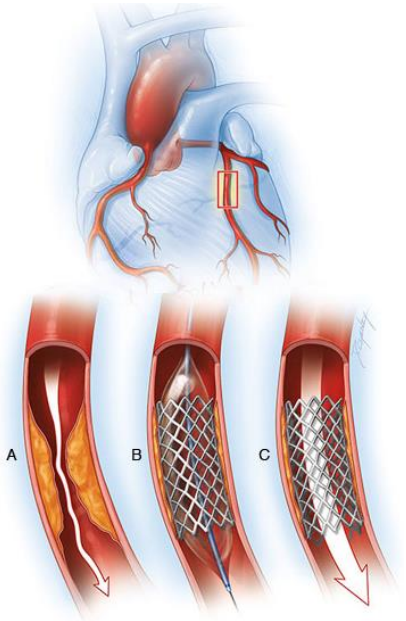

Figure 2.3: Stent deployment procedure: **a)** restricted blood flow in a stenotic artery, **b)** balloon on tip of catheter is inflated to expand the stent, **c)** expanded stent after removing catheter and deflated balloon [4]

INTRAVASCULAR OPTICAL COHERENCE TOMOGRAPHY

Intravascular Optical Coherence Tomography (IVOCT) is a newly developed imaging modality that provides high resolution, cross sectional images of vascular structures.

OCT principles

The principle of OCT imaging is analogous to that of ultrasound imaging except that OCT uses light waves. The advantages of OCT over sound originate in the much shorter wavelength and substantially higher frequency. An optical beam is scanned across the tissue, measuring the echo time delay and intensity of backscattered light from tissue structures [11]. Since the speed of light is extremely fast, the echo time delay cannot be measured directly, which requires using interferometry techniques. One method is low-coherence interferometry which measures the echo time delay and intensity of backscattered light by interfering light from a sample with light that has traveled a known reference path length and time delay [12]. Measurements are performed using a Michelson-type interferometer where light from a source is directed to a beam splitter; one beam is incident on the sample, while the second beam travels a reference path with variable path length. The backscattered light from the sample is interfered with reflected light from the reference arm at the interferometer output. Interference occurs when the two path lengths match within the coherence length of the light. The measured echo time delay and intensity of the backscattered light yield an axial backscattering profile called A-scan (Figure 2. 4-a). The incident beam is scanned at several lateral positions to produce a two dimensional data set, called a B-scan which represents a cross section of the tissue (Figure 2. 4-b).

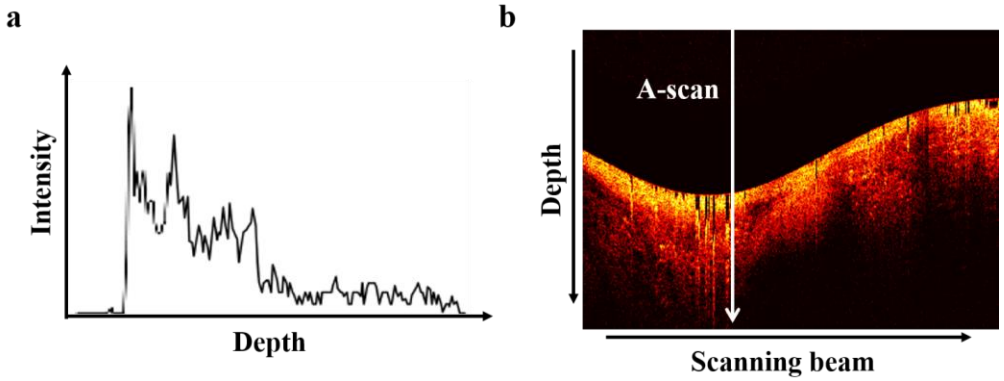

Figure 2.4: **a)** One A-scan, intensity measured vs. depth, **b)** collection of A-scans form a two-dimensional B-scan which represents a cross-sectional view of the tissue.

The axial resolution is determined by the coherence length of the light source. The interference signal is the auto-correlation of the light source where the envelope is equivalent to the Fourier transform of the power spectrum. Since coherence length is the spatial width of the auto-correlation function, it is inversely proportional to the width of the power spectrum. The axial resolution Δz for a source with a Gaussian spectral distribution is given by:

$$\Delta z = \frac{2\,ln2}{\pi}\frac{\lambda^2}{\Delta\lambda} \qquad (2.1)$$

where Δz and $\Delta\lambda$ are the full-width-half-maximum of the auto-correlation function and power spectrum respectively, and λ is the center wavelength. The transverse resolution is determined by the focused spot-size defined by:

$$\Delta r = \frac{4\lambda}{\pi}\frac{f}{d} \qquad (2.2)$$

where d is the spot-size on the objective lens and f is the focal length. In addition, the transverse resolution is also related to the depth of focus which is two times the Raleigh range as given by:

$$2z_R = \frac{\pi \Delta x^2}{2\lambda} \qquad (2.3)$$

IVOCT imaging

IVOCT catheter is directed to the area of interest through a guide wire and IVOCT signal is recorded while the catheter is pulled back in the posterior to anterior directions. The catheter also rotates during data acquisition which combined with translation results in imaging a helical trajectory. However, the presence of blood inside the vessel lumen will strongly attenuate the IVOCT signal due to light scattering. To overcome this problem, a fluid - usually a contrast agent - is flushed around the catheter to clear the blood, eliminate light scattering and enable the light to travel from catheter to the blood vessel lumen and backscattered light into the catheter. Once the pullback is complete, blood flow is restored. IVOCT uses near-infrared light of 1320 μm wavelength, where hemoglobin absorption is low and scattering is reduced, allowing deeper penetration in tissues. Resulting images provide resolution of 10-20 μm and a penetration depth of 2-3 mm.

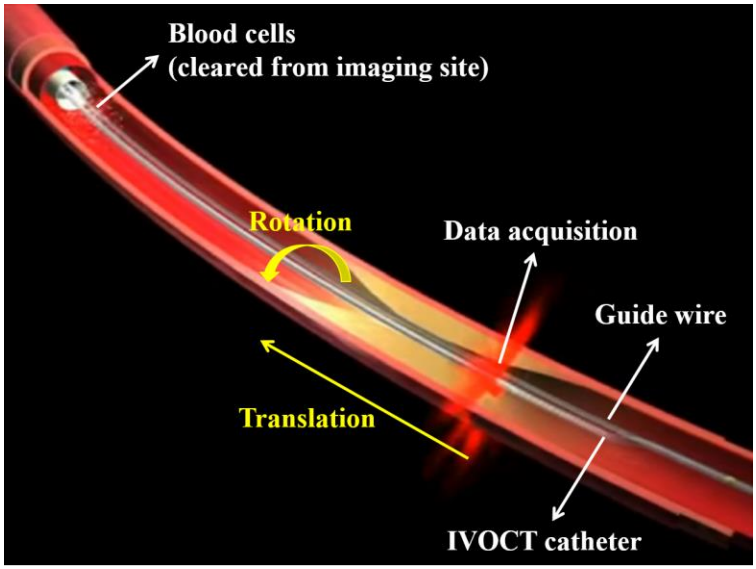

Figure 2.5: Imaging a stenotic artery by IVOCT: catheter is directed to the area of interest through a guide wire, contrast clears the blood and IVOCT signal is recorded while the catheter rotates and is pulled back [13].

Since A-scans are recorded while the catheter simultaneously rotates and translates, two successive A-scans correspond to an angular sweep over the tissue and therefore IVOCT B-scans represent a polar image. To obtain IVOCT images that provide cross-sectional view of a blood vessel a polar to rectangular conversion is required (Figure 2.6). Recorded A-scans during each revolution are distributed evenly over 2π, giving each A-scan the angle of

$$\theta_i = \frac{2\pi\, n_i}{\mathrm{n}} \qquad (2.4)$$

Where n_i is the A-scan number and n is the total number of A-scans. Coordinate location of each point on an A-scan was calculated by

$$x_i = d_i \cos\theta_i \ , \ y_i = d_i \sin\theta_i \qquad (2.5)$$

where x_i and y_i are the coordinate locations in Cartesian coordinate and θ_i and d_i are the angle and distance in polar coordinate. Points not obtained through conversion are interpolated by averaging the neighboring points.

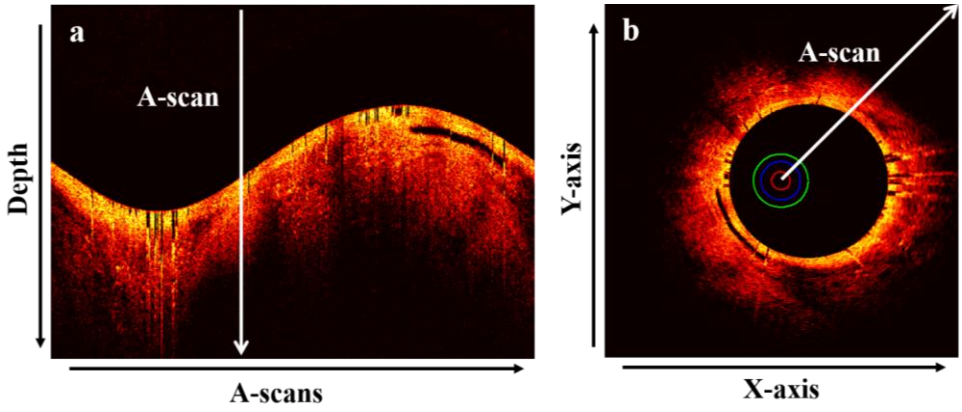

Figure 2.6: a) Polar IVOCT B-scan, **b)** Rectangular IVOCT image

APPLICATIONS OF IVOCT IN STENTING

Angioplasty, in practice for over 40 years, offers a general look at the coronary arteries and can locate occlusion sites, however; the method is not capable of providing the detailed information required to assess the arterial walls in patients undergoing coronary stenting. One of the causes of stent restenosis is poor stent apposition; that is when the stent has not been expanded fully within the artery. Physicians, concerned with injuring the artery with balloon inflation, can end up under-inflating the balloon and stent. Accurate measurements of the diameter of the arterial lumen assist the selection and sizing of stents and balloons [14]. Once the stent has been deployed, further assessment is required to examine the stent struts in relation to the arterial wall and plaque. If the stent has been undersized, a larger balloon can be directed to it and expanded to fit the stent optimally. Furthermore, post deployment follow-ups are required to examine the degree of restenosis within a few months after the procedure [14].

Intravascular Ultrasound (IVUS) have been incorporated into catheterization labs to assist with coronary stenting [15-18]. IVUS uses echocardiography: ultrasonic waves of 20-50 MHz frequencies are emitted by a transducer and reflect from the various tissue structures and the echo of these waves is converted into an image. The transducers are placed on the tip of a catheter which is slipped into the coronary arteries over the same guide wire that is used to deploy the stents and provides a cross-sectional view of the artery. IVUS provide images with resolution of 80-120 μm and penetration depth of 4-7 mm.

IVOCT provides images of coronary arteries with axial resolution of 10-20 μm and tissue penetration depth of 1.5-2.0 mm. Although IVOCT does not penetrate tissue as deep as intravascular ultrasound (IVUS), finer image resolution of one order-of-magnitude allows IVOCT to provide information that IVUS cannot offer and therefore gives this

imaging modality important advantages as an assessment technique for coronary stenting [19-24].

Figure 2.7-a and b illustrate IVUS and IVOCT images of a coronary stent at the same site. Stent struts' positions and orientations relative to the vessel wall are more distinct on the image acquired by IVOCT compared to IVUS, making it easier to identify underdeployed stents. Figure 2.7-c and d compare IVUS and IVOCT images of neoitimal layer covering a Sirolimus-eluting stent at the same cross section. Where IVUS cannot detect neointimal layers in the majority of Sirolimus-eluting stents at the chronic phase, IVOCT is able to detect thinner neointima.

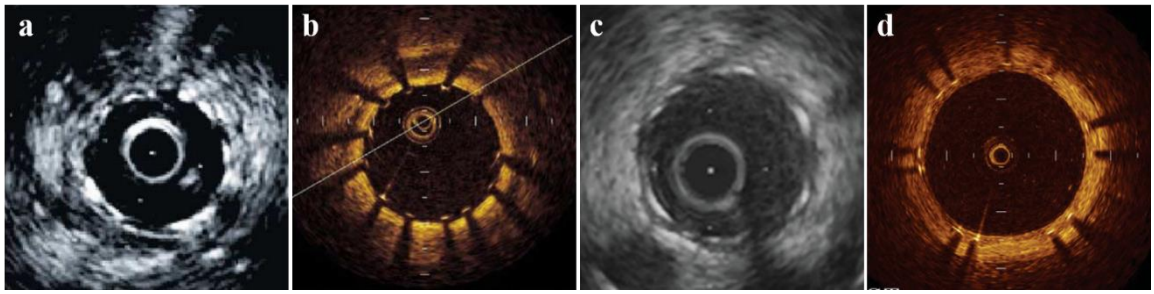

Figure 2.7: Stent image of Right coronary artery (RCA) obtained by **a)** IVUS, **b)** IVOCT [25], cross-sectional images of SES at 6-month follow-up obtained by **c)** IVUS and **d)** IVOCT [26]

IVOCT IMAGING ARTIFACTS

There are several artifacts associated with the images produced by IVOCT systems some of which are common to both IVOCT and IVUS. These artifacts were first stated by Bezerra et al [26].

- Residual blood: results in attenuation and scattering of the IVOCT light beam, leading to a poor image quality (Figure 2.8-a).

- Saturation artifact: occurs when amplitudes of the reflected light from a highly reflective surface (stent struts) exceeds the dynamic range of the data acquisition system and gives rise to "streamers" (Figure 2.8-b).
- Sew-up: artifact is a single point misalignment of the lumen border, resulting from rapid artery or imaging wire movement between successive B-scan in the pullback (Figure 2.8-c).
- Bubble artifact: occurs when small gas bubbles are formed in the silicon lubricant used to reduce friction between the sheath and the revolving optic fiber in OCT systems. It can attenuate the signal along a region of the vessel wall, and images with this artifact are not suitable for tissue characterization (Figure 2.8-d).
- Nonuniform rotational distortion (NURD) is the variation in the rotational speed of the catheter which results in the distortion of the image.

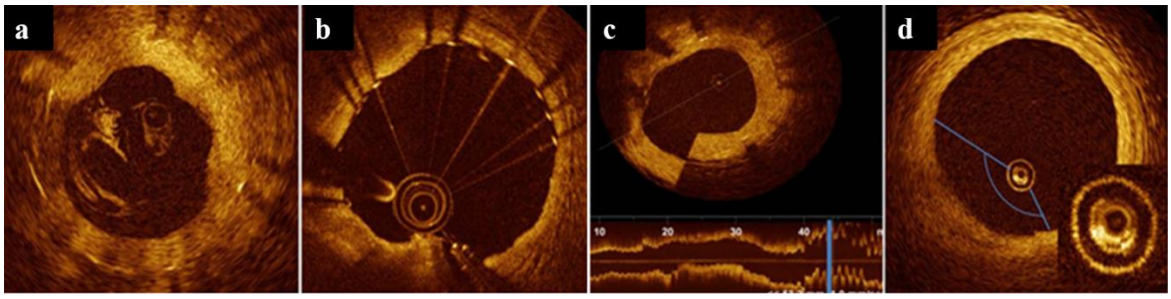

Figure 2.8: IVOCT imaging artifacts **a)** residual blood artifact, **b)** saturation artifact, **c)** sew-up artifact, **d)** bubble artifact [26]

- Sunflower artifact: refers to the 'bending' of the stent struts towards the catheter - analogous to a sunflower bending toward the sun. Sunflower effect occurs when the catheter is at eccentric positions in the vessel lumen and is most pronounced when the catheter is adjacent to the luminal wall. The metal struts appear as a straight line, perpendicular to the imaging light beam and may be obliquely oriented

to the luminal wall which makes well-opposed stent struts appear poorly opposed (Figure 2.9-a).

- Merry-go-round effect: referred to the elongation of the stent strut which is due to the combination of an eccentric catheter position and scattering of the light beam caused by residual blood (Figure 2.9-b).

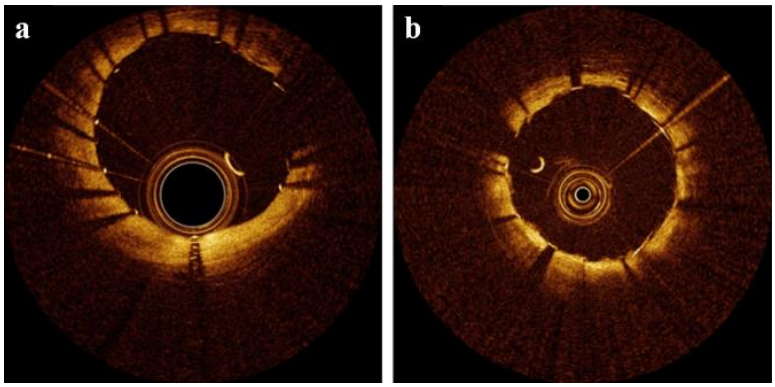

Figure 2.9: a) sunflower artifact, **b)** merry-go-round artifact

Among the aforementioned artifacts, the sunflower and merry-go-round effects have a great impact in assessment of coronary stents. Due to the tortuosity of the arteries, the catheter is often adjacent to the vessel wall during a pullback which inevitability results in these artifacts. Considering the significance of the misinterpretation of IVOCT images, development of a correction scheme is necessary. This can be achieved by first understanding the mechanism of the artifacts and successfully reproducing them.

Chapter 3: Models for studying IVOCT artifacts

To characterize IVOCT imaging artifacts two models were created; a physical blood vessel model to acquire images under controlled conditions and a computer model using physical and physiological based parameters to perform optical simulations.

PHYSICAL BLOOD VESSEL MODEL

Phantom blood vessels were constructed with elastic and optical properties comparable to arterial walls. Coronary stents were deployed within phantom vessels and were imaged by Micro-CT as a reference. IVOCT images of phantom vessels with deployed stents were acquired to examine artifacts.

Phantom vessel material

The base material was polydimethylsiloxane (PDMS) which is available as an unpolymerized liquid resin with a separate curing agent. PDMS is optically clear with refractive index (n_d) of 1.40 [27], slightly higher than that of tissue (n_d = 1.34). Titanium dioxide (TiO_2) is a highly effective scatterer that is available as a white powder with different particle sizes. Depending on the desired scattering coefficient (μ_s), a specified amount of TiO_2 was added to the liquid PDMS and mixed with the curing agent which resulted in the material setting to form a stable solid.

Scattering coefficient measurement

To determine the required amount of TiO_2 to obtain desired scattering coefficients, a mix of PDMS and TiO_2 at specific concentration was spread on glass slides, forming thin layers of controlled thicknesses. After allowing samples to cure for 24 hours, transmitted light through the samples was measured by a spectrometer. Since PDMS absorption in near-infrared range is negligible [28], total loss is considered the result of scattering by

TiO_2 particles. The relationship between transmitted light fraction and the scattering coefficient is given by

$$T(z) = e^{-\mu_s z} \qquad (3.1)$$

where T is the transmitted light fraction, z (mm) is the distance light travelled (film thickness) and μ_s (mm^{-1}) is the scattering coefficient. By replacing the measured values of T for known z thicknesses, μ_s was calculated and averaged. The relationship between scattering coefficient and concentration is given by

$$\mu_s = \rho\, \sigma_s \qquad (3.2)$$

where μ_s (mm^{-1}) is the scattering coefficient, ρ (mm^{-3}) is the number concentration and σ_s (mm^2) is the scattering cross section. Having found μ_s corresponding to TiO_2 concentration used in the measurements and considering their linear relationship, required concentrations for different μ_s values can be determined. Scattering strength of biological tissues are reported by measuring reduced scattering coefficient (μ_s') which is related to μ_s by

$$\mu_s' = (1 - g)\, \mu_s \qquad (3.3)$$

where g is anisotropy factor which represents the average direction of scattered light ($g = \langle \cos\theta \rangle$). PDMS demonstrates isotropic scattering (g = 0.5) [29] whereas biological tissues are highly forward scattering with $g \approx$ 0.8-0.9 [30].

Blood vessel phantom fabrication

A mold for the phantom vessel was constructed of aluminum and brass as illustrated in Figure 3.1. The cylindrical aluminum housing has two parts that fixed the outer diameter of phantom vessels at 6mm and length of phantom vessels at 25 mm (Figure 3.1-a).

Aluminum halves fit together with two steel pins (Figure 3.1-b) and cylindrical brass post inserts into an aluminum base to form mold for inner vessel lumen (Figure 3.1-c). Two brass cylinders with diameters of 3 mm and 4 mm were fabricated to give lumen diameters of 3 and 4 mm. Aluminum base plate fastened to joined-aluminum halves with two steel screws (Figure 3.1-d).

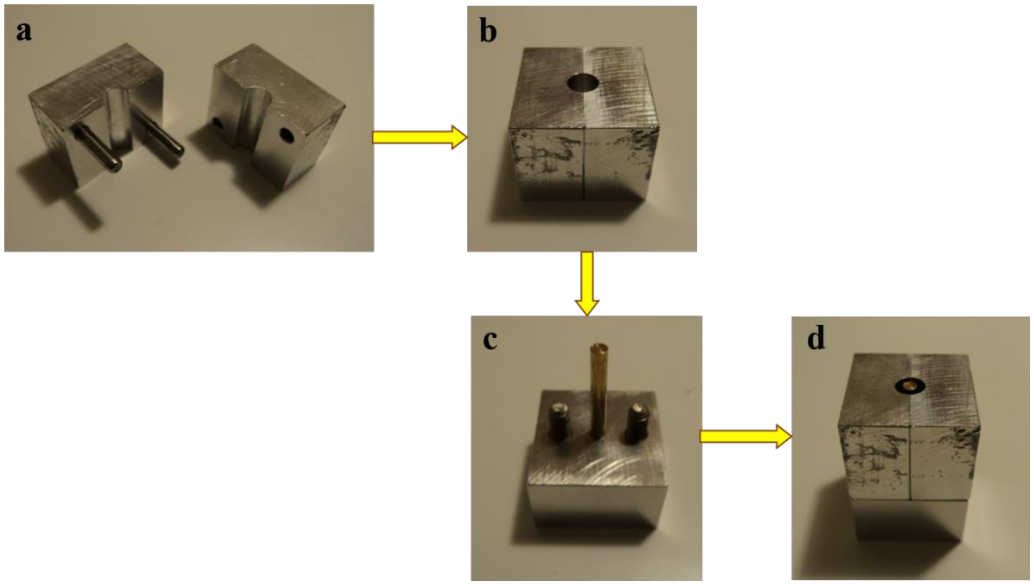

Figure 3.1: Mold to construct phantom blood vessels, **a)** cylindrical aluminum housing, **b)** steel pins fit halves together, **c)** cylindrical brass post, **d)** aluminum base plate fastened to joined-aluminum halves.

Phantom mix was prepared with PDMS and a curing agent. PDMS and curing agent were mixed in ratio of PDMS to curing agent of 10:1. Titanium dioxide (5 mg/ml) was added to the PDMS-curing agent mix at 5 g TiO_2 per 1 liter PDMS/curing agent mix. The mix was poured into the mold and placed in a vacuum chamber at -25 psi gauge pressure for approximately 30 minutes to remove bubbles, and allowed to cure for 24 hours. The two aluminum halves were taken apart from the sides, leaving the phantom on the base

with the brass cylinder in the middle. The phantom was pulled along the axis of the brass cylinder until it was completely removed (Figure 3.2-a).

Stent deployment within phantom vessels

Metallic drug-eluting stents that were utilized in this study include 3.0×8mm CYPHER® Sirolimus-eluting stent (Cordis), 3.0×9 mm Endeavor® Zotalorimus-eluting stent (Medtronic), 3.0×8 mm TAXUS® Liberte® Paclitaxel-eluting stent (Boston Scientific), 3.5×8 mm TAXUS™ Express2™ Paclitaxel-eluting stent (Boston Scientific), 4.0×12 mm XIENCE V Everolimus-eluting (Abbott Vacular). In addition, one bioabsorbable stent, a 3.0×18 Absorb™ stent (Abbott Vascular) was also used. Each Stent which is mounted on a balloon was inserted in a phantom vessel and the balloon was inflated at pressure of 16 atm for 30 seconds. Expanded stent stayed inside the phantom while the balloon was deflated and removed (Figure 3.2-b). The bioabsorable stent was deployed within the phantom vessel that was submerged in a water bath at 37 °C body temperature to prevent any structural damage to the polymer.

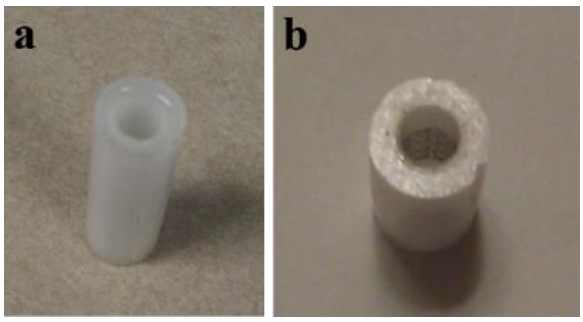

Figure 3.2: **a)** Constructed opaque phantom vessel, **b)** phantom vessel with deployed stent.

Micro-CT imaging

Micro-CT imaging of stents deployed in the phantom vessel were acquired and utilized as a "gold standard" image reference of stent struts' dimensions, position and

orientation relative to the phantom vessel wall. Stents were scanned at the High-Resolution X-ray CT (HRXCT) Facility at The University of Texas at Austin. A FeinFocus microfocal X-ray source operating at 200 kV and 0.17 mA with no X-ray prefilter was employed with an empty container wedge. Micro-CT slice thickness corresponded to one line in a CCD image intensifier imaging system, with a source-to-object distance of 19 mm. For each slice, 1000 views were recorded with two samples per view. Field size of image reconstruction was 6mm, pixel grayscale was adjusted with an offset of 4000 and scale of 300. Each dataset consisted of 1750-2375 slices (depending on the length of the stent) recorded along the long axis of the stent. Each image slice was rendered at 1024×1024 pixel resolution, resulting in an in-plane resolution of 5.86 μm per pixel. Image slices were contiguous each with a thickness of 6.62 μm (Figure 3.3).

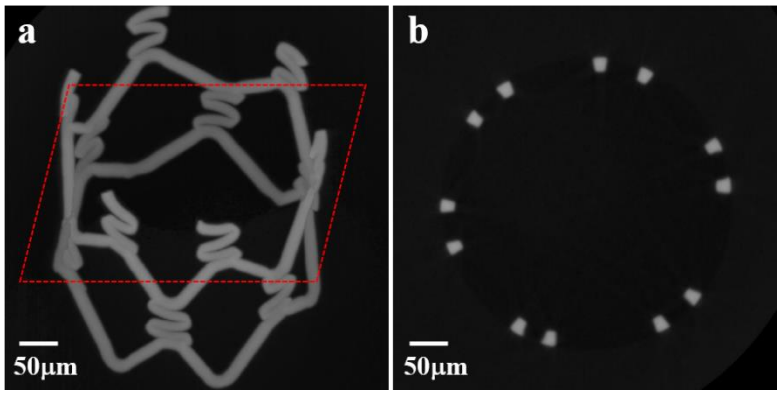

Figure 3.3: Micro-CT images of a CYPHER® stent **a)** three-dimensional reconstruction of a longitudinal portion of a stent, **b)** a cross sectional view of the phantom vessel with pixel size of 5.86μm.

Higher resolution Micro-CT imaging of a stent strut was completed to simulate light interaction between an IVOCT catheter and stent strut. For this work, high resolution close-up scans of a CYPHER® and an Endeavor® struts were acquired using an Xradia microXCT scanner operating at 150 kV and 10 W with no X-ray prefilter employing a 40X

detector. A total of 369 views were acquired over an angular extent of ±92°, integration time for each view was 20 seconds. The object-to-detector distance was set at 9.2 mm while the object-to-source was at 37.5 mm, resulting in 0.53 micron resolution (both in-plane and interslice). To remove instrumentation artifacts from the reconstruction, a reference image consisting of 45 averaged frames was subtracted from each recorded frame. The resulting dataset consisted of 944 slices each with 788×1024 pixels. A three-dimensional representation of the strut was stored in a stereolithography (STL) file format.

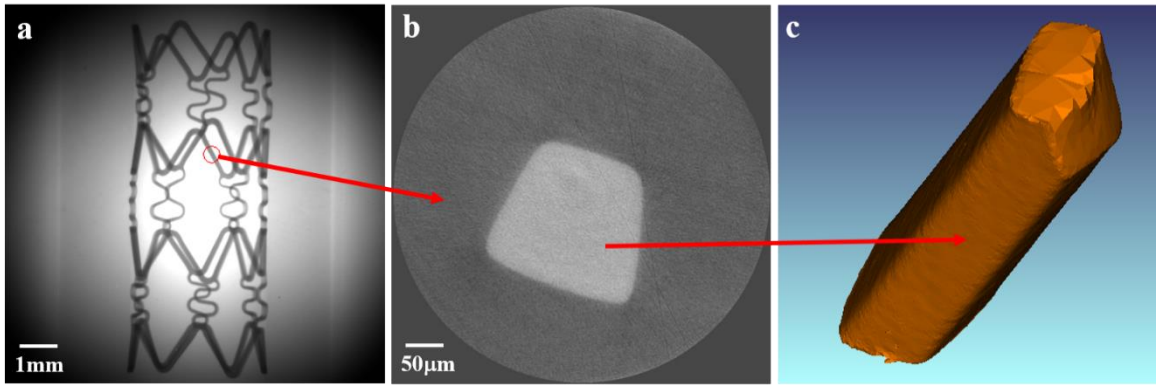

Figure 3.4: **a)** selected strut of a CYPHER® stent, **b)** cross sectional view of the strut, **c)** three dimensional STL of the stent strut.

IVOCT imaging setup

An apparatus was designed to fix position of the phantom vessel while acquiring IVOCT images in presence of a flush fluid (Figure 3.5). The phantom vessel with deployed stent was placed inside a container which was mechanically fastened to two translation stages and two goniometers to adjust position and orientation of the phantom vessel. The catheter attached to a guide wire was passed through the phantom vessel and fixed at both ends and flush fluid was injected with a syringe. Pure saline and mix of saline and goat blood were used as flush fluid for different experiments. Images were acquired using frequency domain IVOCT system (CoreVue, Volcano Corporation, Billerica, MA)

providing 20,000 A-scans per second and frame rate of 30 frame/sec. Before each recording, the tip of the fiber inside the 3.1 French catheter was moved to the region of interest and the length (10-20 mm) and velocity (1-2 mm/s) of the pullback, depending on length of the stent, were specified.

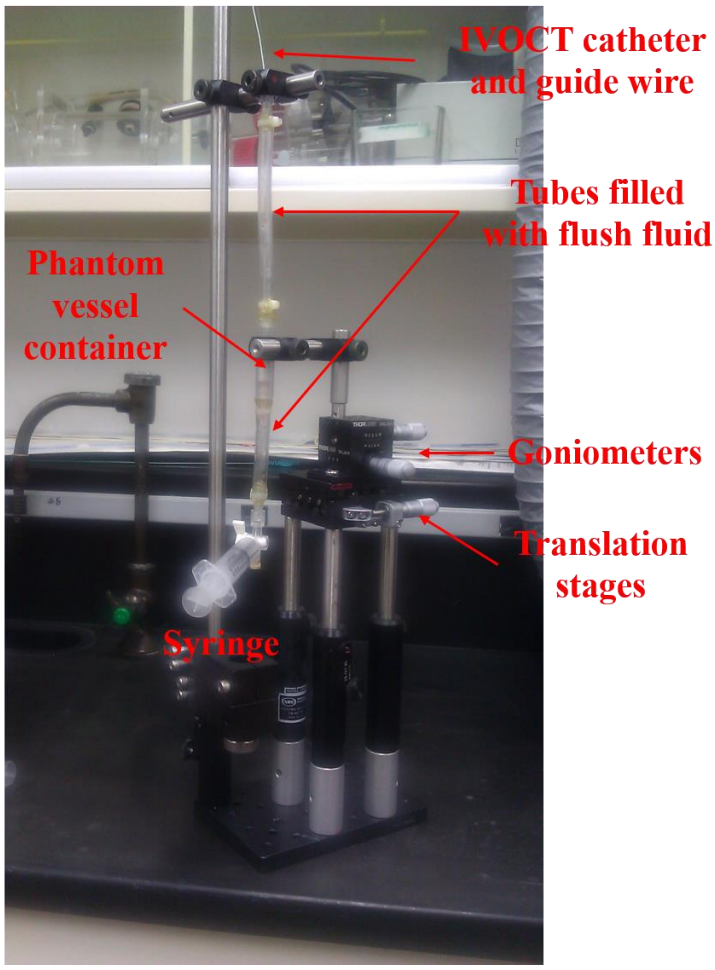

Figure 3.5: IVOCT imaging setup: position and orientation of the phantom vessel (inside the container) was adjusted by translation stages and goniometers. Catheter attached to the guide wire was pulled back through the phantom vessel while flush fluid was injected with a syringe.

Reading IVOCT data in MATLAB

IVOCT raw data are arranged as stacks of B-scans stored in a Datalog file format proprietary to National Instruments (Austin, TX). To access the A-scans, a LabVIEW file reader was written that opens the frames in a pullback one by one and appends each to the end of the binary file. After reading all frames in the pullback, all data is stored in a one-dimensional array containing all A-scans of all frames. This binary file is then opened by a MATLAB reader which allows the user to access a specific A-scan by providing B-scan and A-scan reference numbers using the heather file.

Contrast Group Refractive Index Measurement

Group refractive index of a contrast agent (Omnipaque™, GE Healthcare, Princeton, NJ) at wavelength of 1310 nm was measured using an OCT system [31]. This method was first introduced by Sorin et al. [32] to measure simultaneously group refractive index and thickness and has been applied in refractive index measurement of different tissues [33] and collagen films [34]. For this measurement, a glass capillary with rectangular cross section (4 mm × 0.7 mm) was used to hold the contrast. First, the glass capillary without contrast was positioned under the optical fiber in the sample path of the measuring interferometer [31] and positions of reflections from the various glass-air interfaces recorded. Next, while maintaining the glass capillary in a fixed position, Omnipaque™ (350 mgI/ml) was injected into the lumen of the glass capillary to ensure *OPL* measurements of filled and un-filled capillaries were recorded at the same position.

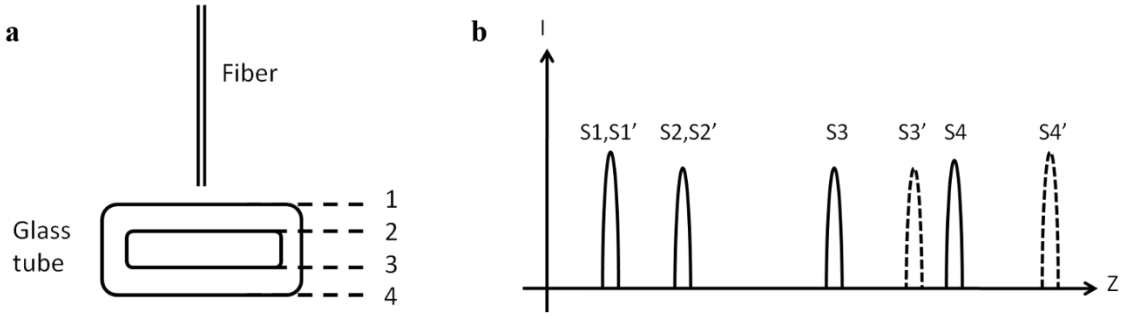

Figure 3.6: **a)** cross sectional view of the glass tube and the optical fiber, 1-4 indicate the interfaces that reflect the light back into the fiber, **b)** S1-4 reflected signals from empty tube, S1'-4' reflected signals when the tube is filled with contrast.

Optical pathlengths of the air-filled (d_{air}) and contrast-filled ($d_{contrast}$) glass capillary lumen are measured by the difference between S3 and S2 and the difference between S3' and S2', respectively. Group refractive index of contrast ($n_{contrast}$) was obtained as the ratio of $d_{contrast}$ to d_{air}, ($n_{contrast} = d_{contrast}/d_{air}$). The measurements were done three times and the average group refractive index of contrast was 1.455.

COMPUTER MODEL

Catheter/strut model

Simulation of light transmission in a 3.1 French IVOCT catheter was achieved using optical design software (Zemax, Radiant, Redmond, WA). The catheter model (Figure 3.7) includes: a point source with cone angle of 6.315° and wavelength of 1310 nm, a single-mode optical fiber (SMF-28 which features low-dispersion at 1310 nm) with mode field diameter of 10 μm [35], a GRIN lens (0.5 mm diameter, 1.32 mm length and peak refractive index of 1.629), 0.150 mm glass (BK7) 45° prism and a polymer sheath (r_o-r_i = 152 μm). In optical simulations, the space (256 μm) between glass prism and sheath is filled with contrast. Simulation of light propagation through the catheter and vessel lumen was completed in a non-sequential ray tracing mode. The light beam initiated at the

source (tip of optical fiber), transmits and is focused by a GRIN lens, enters the prism and is reflected and passes through the sheath and leaves the catheter into the vessel lumen. Lumen space between the outer catheter sheath and stent strut is filled with contrast.

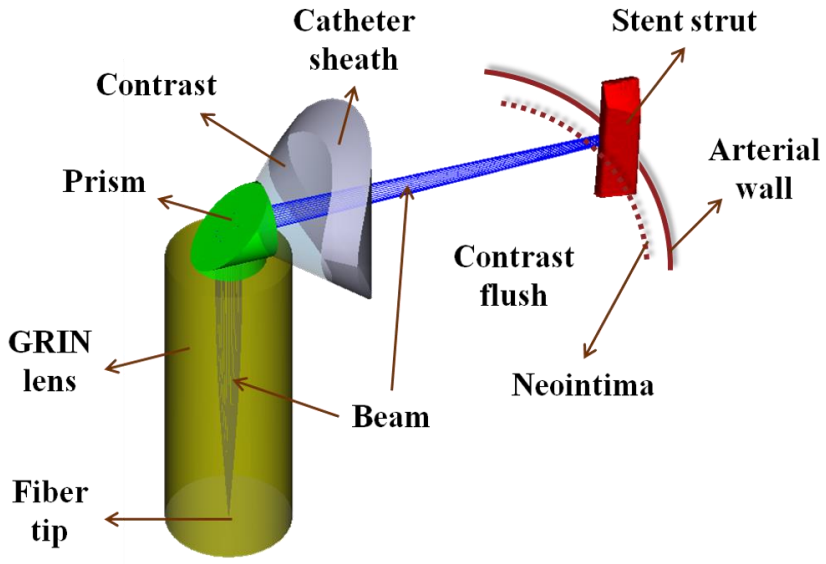

Figure 3.7: Geometry of IVOCT catheter model and stent strut

To simulate the reflection and scattering of light from a stent strut, the stereolithography (STL) object file obtained from Micro-CT imaging was imported into the IVOCT catheter model (Figure 3.7). Arterial tissue was added adjacent to the strut and bulk scattering inside the tissue was modeled using μ_s = 20 mm^{-1} and Henyey-Greenstein phase function [36] which is widely used for the analysis of optical measurements on tissue where g = 0.8. To include roughness of the contrast-vessel interface, Lambertian surface scattering was assumed. Flush fluid in the lumen is weakly scattering with a scattering coefficient of μ_s = 0.2 mm^{-1}, corresponding to a residual 0.1% blood concentration [37]. Specular reflection was assumed for the strut and light backscattered from the strut was collected into a 10 µm diameter pupil and coupled back into the OCT catheter.

Beam spot-size variation

Propagation of light beam through the space is described by a Gaussian profile. This variation of spot-size with distance from the catheter may affect the recorded IVOCT images when the catheter is at eccentric positions. Moreover, the catheter sheath introduces astigmatism aberration which results in the beam focusing differently along the axes. The variation of beam spot-size as a function of distance from the catheter was measured along different axes as illustrated in Figure 3.8, however, Zemax provide geometrical beam-spot size which reaches zero at focus.

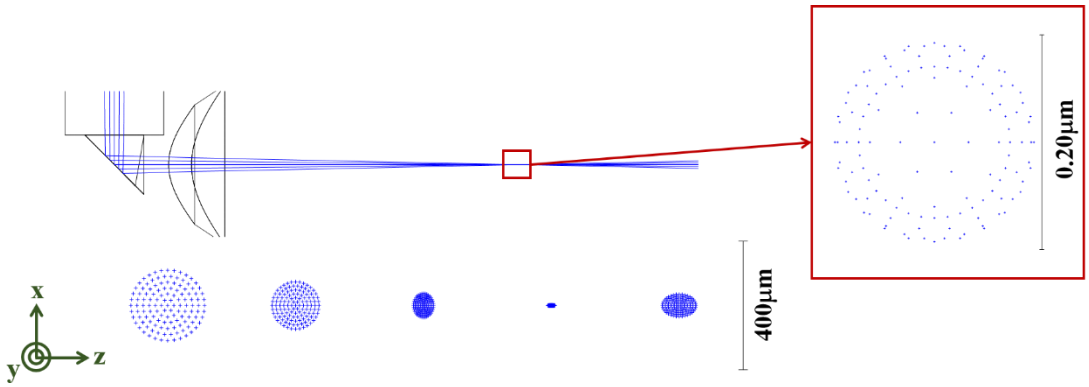

Figure 3.8: Beam profile and spot-size which focuses differently along axes due to astigmatism introduced by catheter sheath, close up: spot diagram at focus reaches 0.

Since the imaging system is diffraction limited, the effect of diffraction on the spot-size was accounted for by obtaining encircled energy plots (Figure 3.9-a). Radius of 10 µm from the center corresponded to 80% of energy which was added to the beam spot-size to include effect of diffraction. The variation of beam spot-size with distance from catheter is demonstrated in Figure 3.9-b. The beam spot-size along x-axis focuses at a distance of 1.5 mm form the catheter whereas it remains almost constant along y-axis.

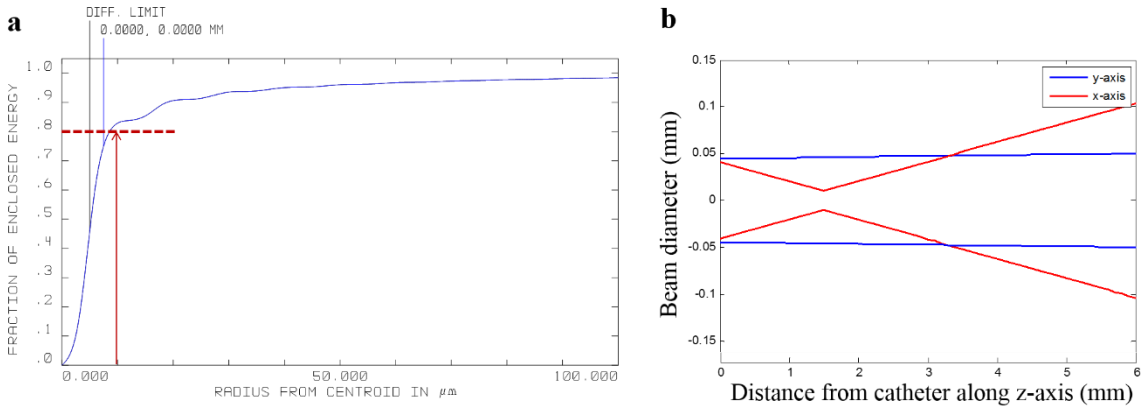

Figure 3.9: **a)** Diffraction encircled energy, **b)** variation of beam spot-size with distance from the catheter along x- and y-axes.

Simulation parameters

Rotation of the IVOCT catheter was simulated in a 3mm diameter vessel lumen. Fiber in the IVOCT catheter was rotated over the strut with an angular range of 20 degrees in 0.5 degree steps and 200,000 rays were traced at each angular position.

To examine the effect of beam size, distance between the catheter and strut was varied along the diameter of the vessel perpendicular to the flat side of the strut, corresponding to catheter offsets from the vessel center of r_c = -0.50, 0.0, 0.50 and 1.00 mm (Figure 3.10-a). To examine the effect of catheter eccentricity, catheter was shifted from the vessel center along the diameter parallel to the flat side of the strut, at catheter offsets from the vessel center of r_c = 0.0, 0.30, 0.60 and 0.95 mm, changing the location of incident beam on the strut (Figure 3.10-b). To examine the effect of neointimal layer, simulation was completed for two cases with thicknesses of 50 and 400 μm covering the stent strut while the catheter was centered (Figure 3.10-c).

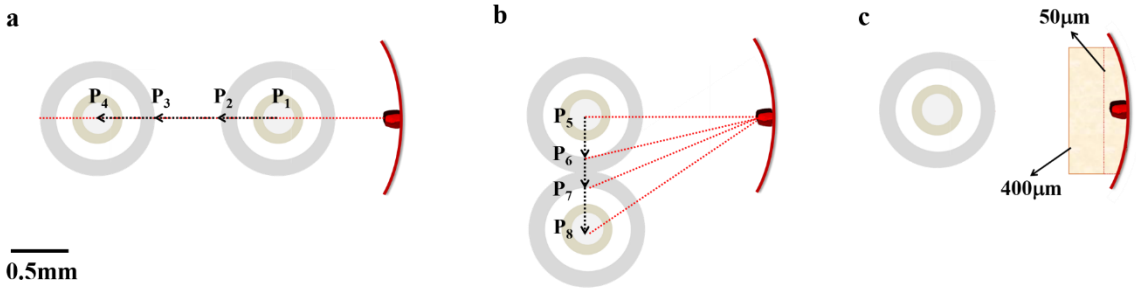

Figure 3.10: Stent strut orientation with respect to IVOCT catheter: **a)** catheter positions along the diameter of the vessel perpendicular to the flat side of the strut, r_c = 0.50 (P_1), 0.00 (P_2), 0.50 (P_3) and 1.00 mm (P_4), **b)** catheter positions along a diameter parallel to the flat side of the strut, r_c = 0 (P_5), 0.30 (P_6), 0.60 (P_7) and 0.95 mm (P_8), **c)** neoinitmal layers of 50 and 400 µm.

Non-sequential ray tracing

At each catheter rotation, as the rays were traced, the ray data was saved to a file specified with a *ZRD* extension. The Ray Database Viewer reads in a *ZRD* file, and displays the data in a text format (Figure 3.11).

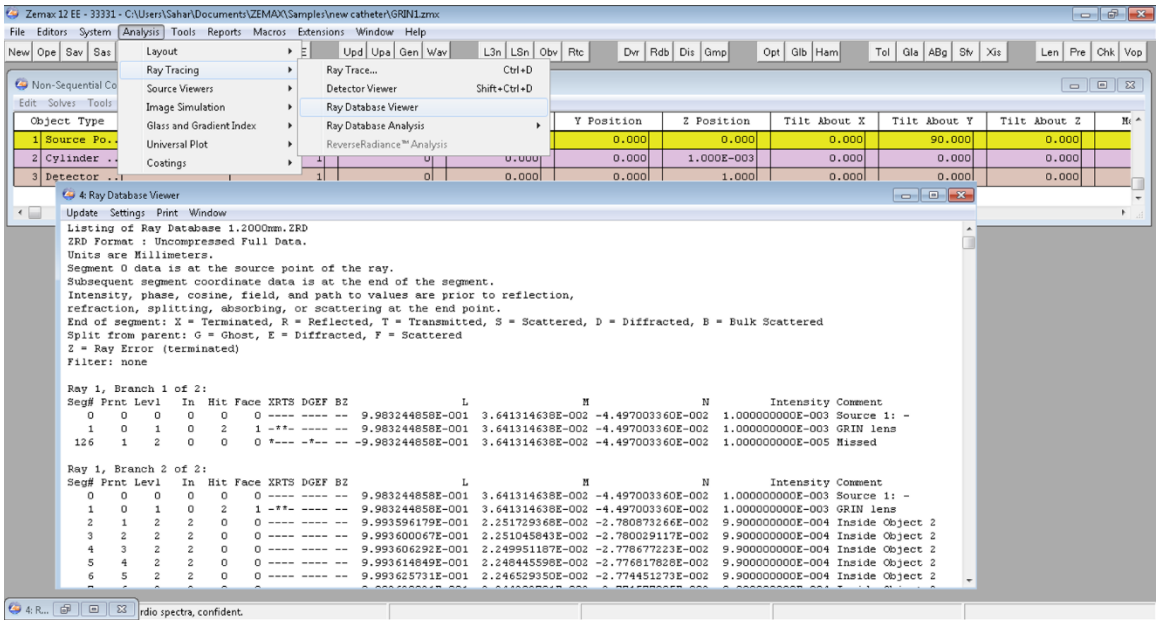

Figure 3.11: Typical ray listing from reading a *ZRD* file.

Seg# is the segment number, the part of the ray that travels through a particular medium, *Prnt* is the parent number, prior segment that generated the particular segment, *Levl* is how many segments away from the source ray the segment is, *In* indicates what object number the segment is traveling through, *Hit* indicates the object number struck at the end of the segment, *XRTS DGEF BZ* is a quick indicator of what happened to the segment. *X* means terminated, *R* reflected, *T* transmitted, *S* scattered, *D* diffracted, and *B* bulk scattered. All these values indicate what happened at the end of the segment. The values *G*, *E*, and *F* indicate whether the segment was a ghost, diffracted, or scattered, respectively, from the parent segment, so these events occurred at the start of the segment. The symbol *Z* indicates a ray error occurred and the ray was terminated. The other data displayed includes the global *XYZ* coordinates of the end of the segment, the global normal vector coordinates of the object struck at the end of the segment, the ray intensity and the object comments. To display only the rays with certain properties, Filter Strings were used which allow definition of a conditions that rays must pass before they are displayed. Filter String syntax indicates if one segment within a ray hit, miss, reflected, refracted, scattered, diffracted, or ghost reflected from an object [38].

In this simulation, the rays that were reflected after hitting the stent strut and travelled back to the tip of the fiber were saved in a *ZRD* file. Parameters that were saved in a text file included coordinate locations on the stent strut of returned rays; intensity and direction-of-cosines of the rays returning to the fiber tip and optical pathlength (*OPL*) of light returning to the catheter.

To simulate rotation of the catheter, position and orientation of strut with respect to catheter were changed for each angular step. To achieve this automatically, Zemax Programming Language (*ZPL*) was used. *ZPL* is a macro language specifically designed for use with Zemax which allows the user to write a particular calculation or graphical

display which is not built in. A *ZPL* macro consists of a series of commands similar to other programming languages, as well as capabilities and functions unique to ray tracing. Figure 3.12 shows an example of a macro used in this study, where for each angular step relative position and orientation of catheter and strut were varied and non-sequential ray trace is completed while Filter Strings are applied to collect desired rays and ray database is stored in *ZRD* file.

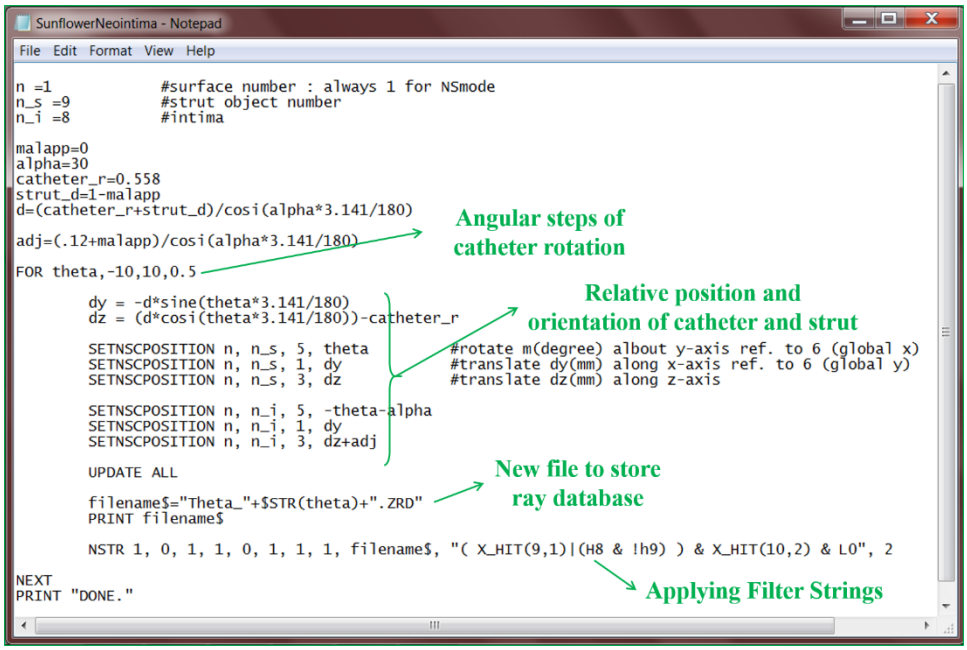

Figure 3.12: Example of a *ZPL* macro to simulate catheter rotation

Data analysis in MATLAB

After opening each *ZRD* file in Ray Database Viewer, ray data was written to a text file. A reader was used to open and import the ray data to MATLAB R2013a (Mathworks, Natick, Massachusetts) for further analysis. Ray presentation as employed in Zemax describes the propagation of light and does not take into account the behavior of wave fronts. The amplitude of light coupled into a single-mode optical fiber is given by

$$A_c = \int_{-\infty}^{+\infty} A_o(r)\, A_f^*(r)\, dA \qquad (3.4)$$

where $A_o(r)$ is the incident beam and $A_f^*(r)$ is the fiber coupling function [39]. Coupling coefficient is defined by integrating the product of phase variation of incident rays (plane waves) and fiber coupling function (Eq.3.5) which characterizes dependence of coupling on the angle of incident beam:

$$c_f = \int_{-\infty}^{+\infty} \Phi_o(r)\, A_f^*(r)\, dA \qquad (3.5)$$

where $\Phi_o(r)$ is the phase variation of the incident ray (plane wave) and $A_f^*(r)$ is the fiber coupling function [13]. Eq.3.5 was solved using Wolfram Mathematica® 9 to find coupling coefficient:

$$c_f = e^{2\pi\sigma^2\left(\cos\theta_x{}^2+\cos\theta_y{}^2\right)/1.32} \qquad (3.6)$$

where σ is the mode-field diameter of the optical fiber, $cos\,\theta_x$ and $cos\,\theta_y$ are direction of cosines of the incident beam along *x* and *y* axes.

Product of coupling coefficient squared and recorded intensity of each ray gives the intensity of coupled light into the optical fiber. The resulting intensities were then convolved with longitudinal point-spread function corresponding to a full-width half maximum Gaussian spectral width of 50 nm. Data was presented in logarithmic scale (dBm) vs. depth in microns. A polar-to-cartesian conversion was performed on the A-scans to obtain simulated IVOCT images.

Chapter 4: IVOCT measurement of size and apposition of metallic stents

Metallic stent struts typically appear as small bright line-segments in IVOCT images due to light reflection from the metal surface and are inconsistent with the true stent strut surface profile. Vessel curvature and tortuosity frequently result in placement of the IVOCT catheter in an eccentric position in the lumen, giving rise to stent artifacts including the sunflower and merry-go-round effects [26]. For instance, the size of a strut can appear smaller in IVOCT images acquired from an offset (Figure 4.1-b) compared with a centered (Figure 4.1-a) catheter position. In this chapter, effect of beam size and catheter position on the apparent size and apposition of metallic stent struts in IVOCT images were examined.

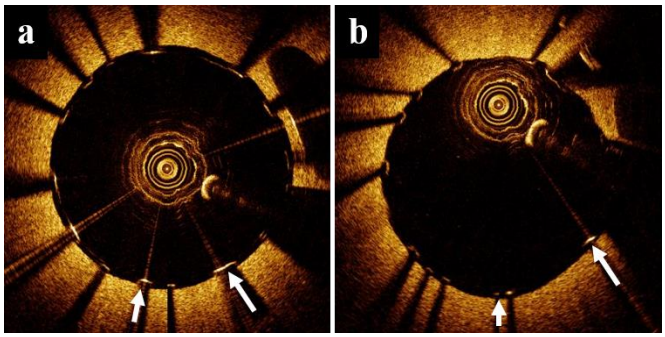

Figure 4.1: Apparent strut size in a phantom: **a)** centered catheter, **b)** eccentric catheter where strut size varied (both arrows) and sunflower artifact is observed (large arrow)

EFFECT OF SPOT-SIZE

Variation in apparent strut size in IVOCT images due to beam-size change was examined by positioning the catheter at different distances from the strut in the Zemax computer model. When shifting the catheter from positions P_1 to P_4 (Figure 3.10-a), as the distance between the catheter and the strut increases, the measured size of the strut in the

IVOCT image varies non-uniformly; from 135 μm (P_1), 100 μm (P_2), 150 μm (P_3) and 225 μm (P_4) as shown in Figure 4.2. Considering the actual size of the strut is 90 μm, the effect of beam size introduces 60% error at r_c = -0.5 mm, 11% error at r_c = 0 mm, 67% error at r_c = 0.5 mm and 189% error at r_c = 0.5 mm. At increased distances from the beam focus, IVOCT signal amplitude decreases and apparent strut blooming (along the light propagation direction) appears less.

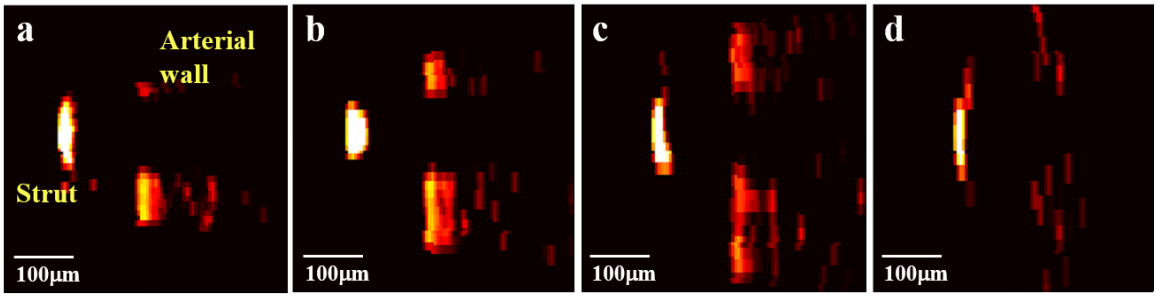

Figure 4.2: Simulated IVOCT images of a CYPHER® stent strut at selected offsets: **a)** P_1 (r_c = -0.5 mm), **b)** P_2 (r_c = 0 mm), **c)** P_3 (r_c = 0.5 mm), **d)** P_4 (r_c = 1 mm).

EFFECT OF STENT SURFACE-SCATTERING PROPERTIES

Intensity of the reflected light back to the IVOCT catheter is partially dependent on the surface-scattering properties of the stent. A Gaussian surface-scattering model (bi-directional scattering distribution function) was assumed for the strut. The expression is given by

$$BSDF(\cos\theta) = A\, e^{\frac{-|\cos\theta|^2}{\sigma^2}} \qquad (4.1)$$

where A is a normalizing constant, angle θ is measured from the normal and the dimensionless value σ determines the width of the Gaussian distribution. The resulting distribution is rotationally symmetric in direction of cosines space, no matter what angle the specular ray makes with respect to the surface normal [38]. Standard deviation of the

direction of cosines of σ = 0.05, 0.25 and 0.5 was assumed where increasing values of σ corresponds to rougher strut surfaces with higher scattering. Reflectivity was measured as the number of returned rays divided by the total number of incident rays.

Reflectivity vs. catheter beam angle for increasing values of σ are shown in Figure 4.3. Stents with less surface scattering have higher reflectivity with the maximum peak of 0.77% corresponding to σ = 0.05 and consequently, appear brighter in the recorded IVOCT images.

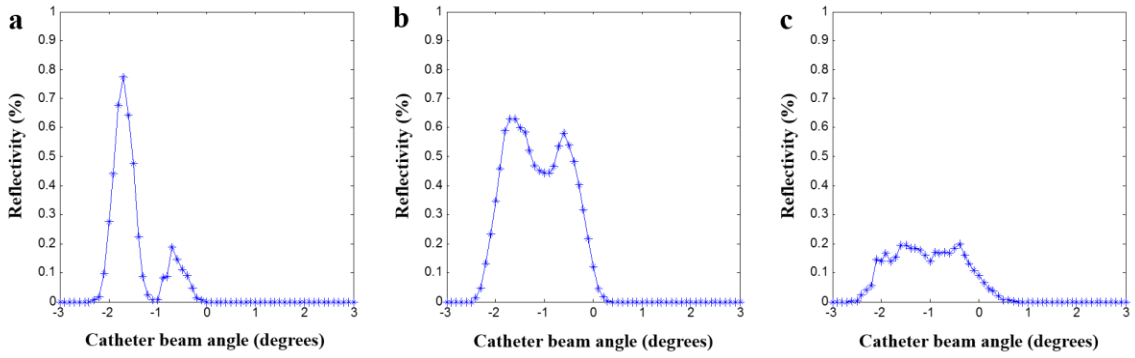

Figure 4.3: Reflectivity vs. catheter beam angle for different bi-directional scattering distribution functions (see Eq. 1.3): **a)** σ = 0.05, **b)** σ = 0.25, **c)** σ = 0.50.

The angular spread of reflected light coupled back into the IVOCT catheter becomes broader as σ increases, increasing from 2.3° to 3.4° of catheter rotation (Table 4.1). Therefore, stents with a broader BDSF surface scattering (larger result in the appearance of wider stent struts in IVOCT images.

$\boldsymbol{\sigma}$	$\Delta\boldsymbol{\alpha}(°)$	$\boldsymbol{R_{max}}(\%)$
0.05	2.3	0.77
0.25	2.8	0.63
0.50	3.4	0.2

Table 4.1: Standard deviation of the direction of cosines (σ) for different stent surface-scattering; beam angular spread ($\Delta\alpha$) of reflected light returned to the catheter and reflectivity (R_{max}).

Simulation results demonstrate that surface-scattering properties of stents impact the reflectivity and apparent size of the strut in IVOCT images. The result also suggests that modifying the surface scattering features of stent struts is a candidate approach of controlling IVOCT imaging artifacts.

EFFECT OF POLAR TO RECTANGULAR TO TRANSFORM

The conversion from polar B-scans to rectangular IVOCT images can introduce an anisotropic shape transformation. Magnitude of the anisotropy is dependent on a number of factors including: 1) number of A-scans in a B-scan; 2) number of axial points in an A-scan; and 3) pixel format of the polar IVOCT image; and 4) distance from the catheter center. Polar B-scan data (Figure 4.4-b) corresponding to the image acquired at an eccentric catheter position contains more pixels in the radial direction (horizontal) and fewer pixels in the angular direction (vertical) compared to the corresponding rectangular IVOCT image. In the coordinate transformation, features in the polar B-scan image appear compressed axially and stretched azimuthally in the rectangular IVOCT image. In case of a specified strut (Figure 4.4, black circle) the circular-shaped strut in the polar B-scan data (Figure 4.4-b) transforms to an ellipse with anisotropy of 3.5 in the rectangular IVOCT image (Figure 4.4-a). Since radial scale is constant, the aspect ratio of the strut in IVOCT image depends on the angular scale which is directly proportional to the distance of the strut from the catheter center. Because this anisotropy may be greater than 1, the coordinate

transformation from polar B-scan data to rectangular IVOCT images is a factor contributing to the sunflower effect.

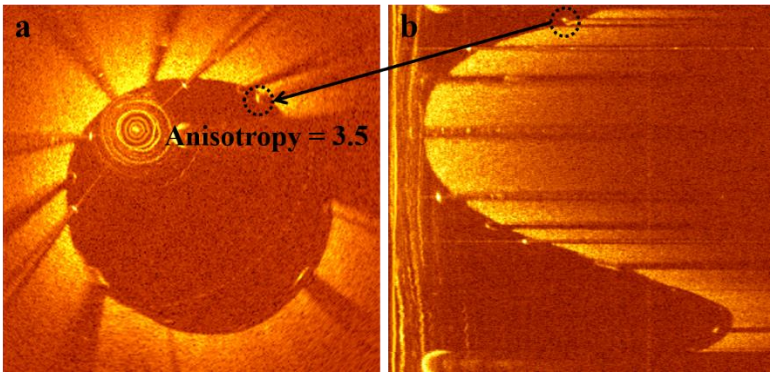

Figure 4.4: **a)** IVOCT image of phantom vessel with eccentric catheter, black circle marks position of one strut, **b)** corresponding polar B-scan data

SUNFLOWER EFFECT IN IVOCT IMAGES OF PHANTOM VESSELS

To observe the sunflower effect and dependence on catheter eccentricity, IVOCT images of the phantom vessel with deployed stents were recorded. At a fixed longitudinal position the catheter was first positioned at the center of the phantom vessel lumen; while translating towards the vessel wall IVOCT images were recorded. Figure 4.5 illustrates sunflower effect; while all stent struts appear well-opposed to the vessel wall when the catheter is centered, at an eccentric catheter position some struts appear in the recorded IVOCT image as a straight line perpendicular to the light beam and obliquely oriented to the luminal wall. The apparent struts lifting off the vessel wall may result in some IVOCT users erroneously concluding the stent is malopposed.

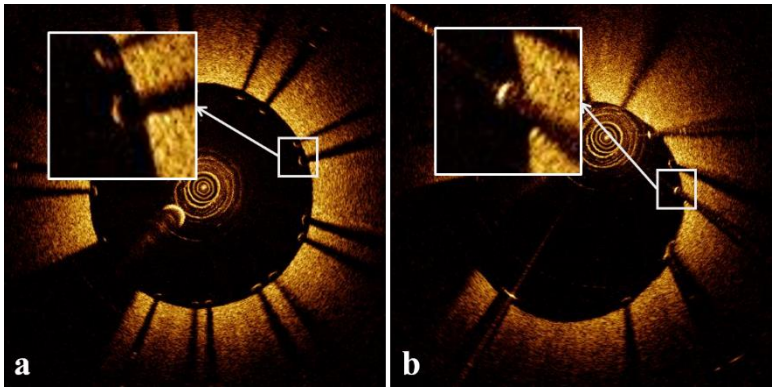

Figure 4.5: **a)** IVOCT image of phantom vessel with centered catheter, **b)** IVOCT image of phantom vessel with eccentric catheter; Note some stent struts "bend" toward the light demonstrating sunflower effect

SIMULATION OF SUNFLOWER EFFECT

Size of the strut region reflecting light into a contrast-filled 3.1 French catheter at the four catheter eccentric positions (P_5-P_8) was computed (Figure 3.10-b). Results suggest that lateral size of the strut region reflecting light back into the IVOCT catheter can be smaller than the incident beam size. Figure 4.6 illustrates the stent strut orientation with respect to catheter at four different eccentric positions and the incident beam size (red) and the regions reflecting light back into the catheter (yellow) at each position. At each of the catheter offsets considered, optical pathlength (*OPL*) of light returning to the catheter over the beam angular spread is nearly constant with a maximum standard deviation of 15 μm.

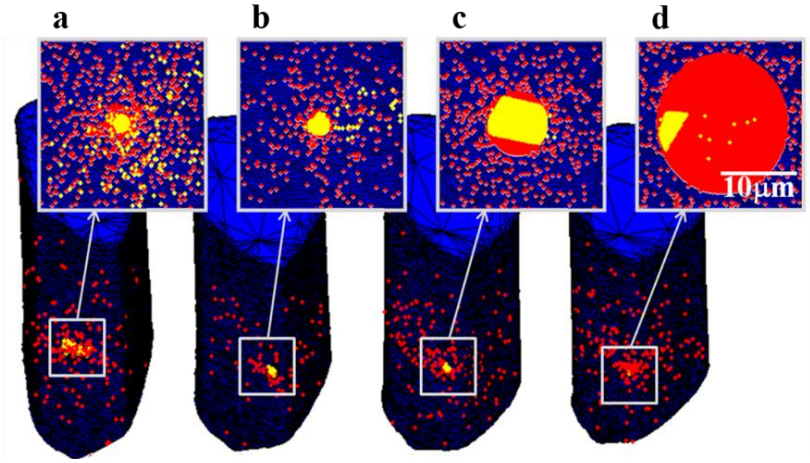

Figure 4.6: Stent strut orientation with respect to IVOCT catheter, incident beam (red) and regions on strut reflecting light back into the catheter (yellow) at: **b)** P_5 (r_c = 0 mm), **c)** P_6 (r_c = 0.3 mm), **d)** P_7 (r_c = 0.6 mm), **e)** P_8 (r_c = 0.95 mm).

ORIGIN OF SUNFLOWER EFFECT

The sunflower effect is an IVOCT artifact observed when imaging metal coronary stents deployed in patients during cardiac catheterization and appears as a bending of stent struts toward the imaging catheter - analogous to a sunflower bending toward the sun. Sunflower effect occurs when the catheter is at eccentric positions in the vessel lumen and is most pronounced when the catheter is adjacent to the luminal wall. When an eccentric IVOCT catheter emits light that is incident on a metal stent strut at any angle, returning light to the catheter is reflected from a small-sized region on the metal strut surface (Figure 4.7, black arrow), while other strut surface areas reflect and scatter light away from the catheter (Figure 4.7, gray arrows). As light transmits from the catheter, a finite beam width at the stent strut ensures return reflections are recorded at each angular position. Since reflections return from a small-sized region on the stent strut, echo-time is nearly constant at each angular position and the metal strut appears in IVOCT images as a straight line bending towards the catheter (Figure 4.7, dotted blue line). Therefore, the sunflower effect

can artifactually make stent struts appear poorly opposed when in fact they are well opposed to the luminal wall.

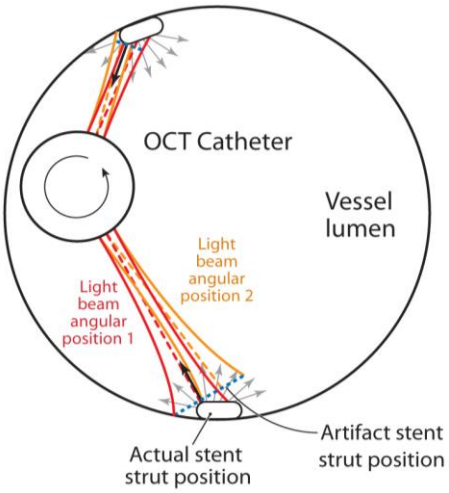

Figure 4.7: An eccentric IVOCT catheter emits light that is incident on metal stent struts at two angular positions.

Complete deployment of coronary stents improves long term patient outcomes, and an early application of IVOCT is to verify full deployment. Although IVOCT provides high resolution images of stent struts to make this assessment, the sunflower effect can erroneously lead to a conclusion of stent under-deployment. Since one does not know - a priori - where on the strut light is reflecting back into the catheter, a fundamental uncertainty is recognized when selecting the point on the apparent strut to measure distance to the vessel wall. Moreover, this uncertainty cannot be resolved without knowledge of the location on the strut that is reflecting light back into the catheter.

MALAPPOSITION MEASUREMENT

Inasmuch as IVOCT stent measurements are at an early stage, no comprehensive consensus methodology exists on how to measure stent malapposition with off-center IVOCT catheter placement that is uniformly agreed upon [40]. In current IVOCT clinical

practice, two approaches are utilized to measure stent malapposition: approach 1) the user draws a line-segment from center of the strut blooming in the IVOCT image to the luminal wall that indicates the shortest distance (Figure 4.8-a), malapposition is determined by subtracting the known strut thickness from the measured distance [41], approach 2) a box representing the strut cross-section is positioned in the IVOCT image so that one box-edge is coincident with the leading edge of the IVOCT strut (blue box in Figure 4.8-b), the user/software draws a line segment from the midpoint of the opposing box-edge to luminal wall that is perpendicular to the box-edge, length of this line indicates strut malapposition [1].

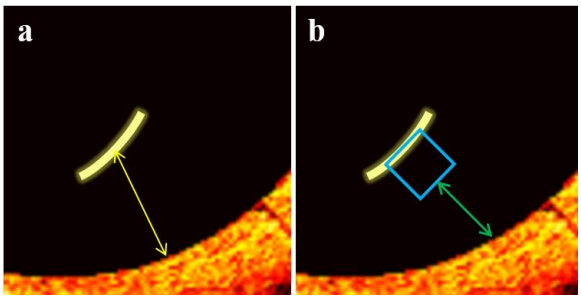

Figure 4.8: Malapposition measurement: **a)** approach 1; yellow line is drawn from center of strut blooming to the luminal wall indicating the shortest distance, **b)** approach 2; box is positioned so that edge is coincident with the leading edge of the stent and green line is drawn perpendicular to the box-edge.

Simulated IVOCT images of a CYPHER® stent strut that is 200 μm under-deployed at catheter positions P_5-P_8 (Figure 3.10-b) are shown in Figure 4.9 where the apparent strut demonstrates the sunflower effect by appearing as a short line (white) directed perpendicular to the incident light beam and obliquely oriented to the luminal wall (Figure 4.9-b to d).

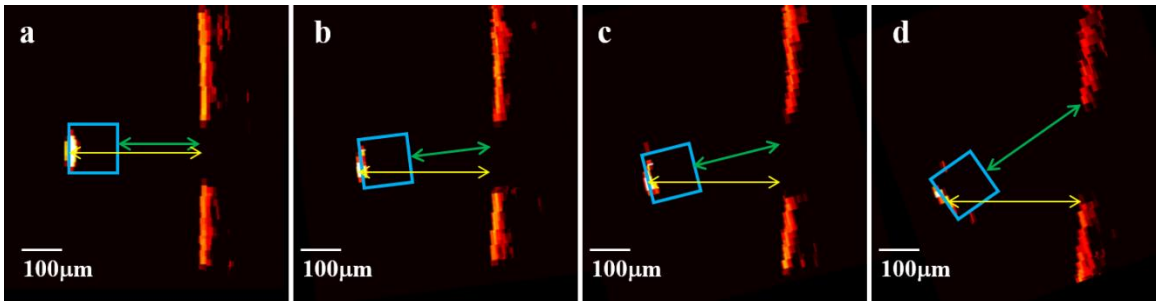

Figure 4.9: Apposition measurements of a CYPHER® stent strut at selected offsets: **a)** P_5 (r_c = 0 mm) **b)** P_6 (r_c = 0.3 mm) **c)** P_7 (r_c = 0.6 mm) **d)** P_8 (r_c = 0.95 mm), yellow line is drawn from center of strut blooming to the luminal wall indicating the shortest distance (approach 1), box is positioned so that edge is coincident with the leading edge of the stent and green line is drawn perpendicular to the box-edge (approach 2).

Strut apposition was measured by the aforementioned two approaches. In approach 1, a line was drawn from center of the strut blooming to the luminal wall (Figure 4.9; yellow lines), malapposition was determined by subtracting the known strut thickness (120 μm) from the measured distances. Measurement errors varied from 4 μm at r_c = 0.0 mm to 1 μm, 4 μm and 7 μm at r_c = 0.30 mm, 0.60 mm and 0.95 mm respectively (Figure 4.9-a to d). In approach 2, a 120 μm thick box was placed along the apparent IVOCT strut and a line segment from the midpoint of the opposing box-edge to luminal wall that is perpendicular to the box-edge, indicating the mal-apposed distance (Figure 4.9; green lines). When the catheter is centered, the measured apposition is equivalent to the actual distance of the strut from the arterial wall. When the catheter is at eccentric positions, the measured appositions for the under-deployed strut produced artifactual errors of increased malapposition: 2 μm at r_c = 0.30 mm, 25 μm at r_c = 0.60 mm and 82 μm at r_c = 0.95 mm (Figure 4.9-b to d).

The two approaches to measure stent apposition give different results for catheter positions P_6-P_8 (Figure 3.10-b). While approach 1 gives accurate apposition measurements

for positions P_6-P_8, approach 2 introduces artifactual errors. Apposition measurement errors introduced when applying approach 2 at positions P_6-P_8 originate from misplacement of the box representing the stent strut. In these cases, placement of the box so that one box-edge is coincident with the leading edge of the IVOCT strut can introduce position and orientation errors. At positions P_6-P_8, light reflects from a small corner or edge region of the stent strut so that strut blooming in IVOCT images is not oriented parallel to the strut edge - thereby introducing the sunflower effect. Alternatively, when the box representing the stent strut is placed correctly (Figure 4.10-a) an accurate apposition measurement is obtained (Figure 4.10-b). In cases when the box is not utilized, approach 1 gives consistent measures of strut apposition and is equivalent to the method first described by Ughi et al. [42] in which the line segment is perpendicular to luminal wall. When utilization of the stent strut box is desired, the box should be positioned parallel to the arterial wall (Figure 4.10-b) with the corner- or edge-region touching the center of the strut blooming in the IVOCT image.

Observation of all stent struts in the IVOCT image can be used for better estimation of orientation and therefore proper placement of boxes. For example, a partially under-deployed stent where the sunflower effect is observed is shown in Figure 4.10-c. To estimate malapposition, a circle is drawn tracing the circumference of the stent and boxes are placed facing the center of the stent. Malapposition is determined by measuring distances from the back surface of the boxes to the luminal wall. Applying approach 1, yellow lines are drawn from the center of strut blooming to the arterial wall perpendicular to the pink circle and the measured malapposition distances match the actual values. Approach 1 provides accurate results in presence of sunflower effect and does not require proper placement of the box representing the strut.

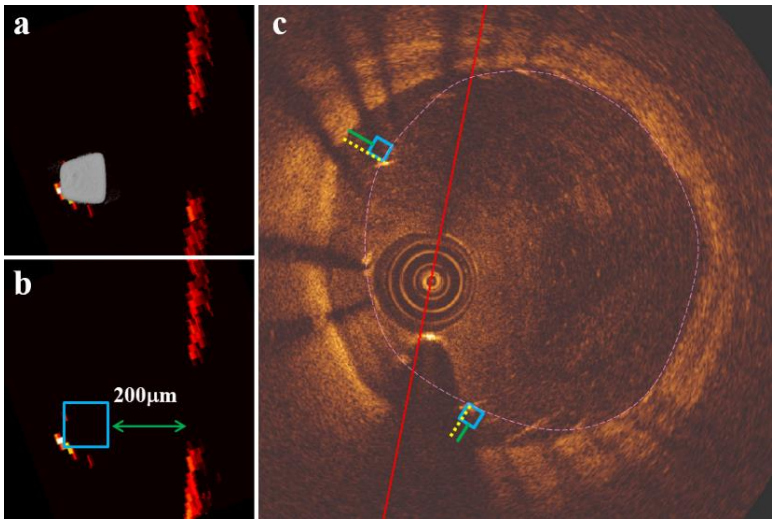

Figure 4.10: a) Actual position of CYPHER® stent strut, **b)** proper box placement provides an accurate malapposition measurement at P_8 (r_c = 0.95 mm), **c)** proper box placement based on distribution of all stent struts for accurate malapposition measurement by approach 2, yellow lines represent malapposition measurement by approach 1.

Chapter 5: IVOCT imaging of coronary artery metallic stents with neointimal coverage

IMPORTANCE OF NEOINTIMA FORMATION

Formation of neointima after stent deployment is an important indicator of vascular healing process. While presence of neointimal layers are desired in the healing response, if the neontimima thickens excessively re-stenosis results - a frequent complication with bare metal stents. To prevent re-stenosis, drug-eluting stents limit neointimal formation by releasing immunosuppressant pharmaceuticals which inhibit smooth muscle cell proliferation (Figure 5.1). In a recent study, CYPHER® and TAXUS® stents resulted in delayed neointimal formation when compared with bare metal stents of similar implant duration [43]. Human pathology studies suggest that the lack of neointimal strut coverage due to delayed vascular healing may be associated with late thrombotic events after stent deployment [44]. Therefore, accurate in vivo assessment of neointimal formation early after stenting may aid in prevention of late stent thrombosis. Although IVOCT offers a superior assessment technique, the clinical significance of a neointimal thickness that is less than or near the axial resolution of the IVOCT system is not well understood. In cases where struts may have partial tissue covering, some investigators consider the strut as covered, whereas others suggest that these struts be classified as having incomplete coverage [40]. A study on accuracy of IVOCT in analyzing the neointimal response to several drug-eluting stents, showed significant variation in the estimation of strut coverage between IVOCT and histology when the neointimal thickness was between 20 to 80 μm [45] which is the range of thicknesses corresponding to thin neointimas formed early after stenting. Issues arising from tissue processing, shrinkage and artifacts associated with histology studies call for further investigations.

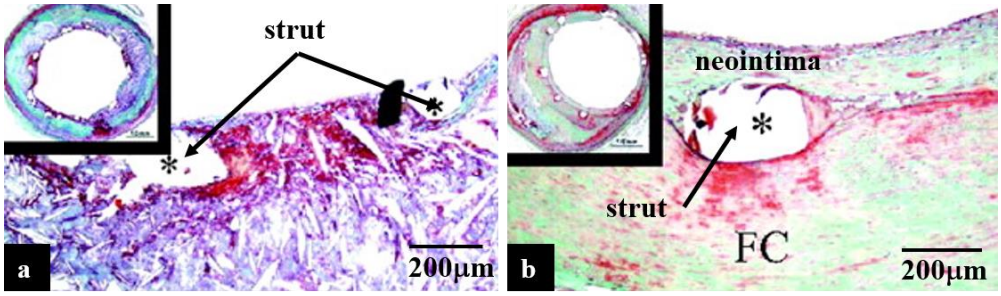

Figure 5.1: **a)** lack of neointima, **b)** desired neointimal coverage [46]

PHANTOM NEOINTIMA FABRICATION

An aluminum mold was built to add neointima coverage to the stent deployed inside the phantom vessel (Figure 5.2). The two pieces of the mold fasten together with a threaded cylinder where the mid-section has a 2.70 mm diameter, providing 150 micron space between phantom vessel wall and outer surface of the mold. Considering thickness of the stent struts, phantom layer covering the stent is 50 microns thick. The two ends have a larger diameter of 3.2 mm to hold the mold inside the phantom and the holes which open to the space between mold and vessel wall, allow injection and extrusion of phantom intimal material. Figure 5.2-b illustrates positioning of the mold inside a translucent phantom vessel. Outer surface of aluminum parts was coated with Teflon to prevent PDMS from sticking to the mold.

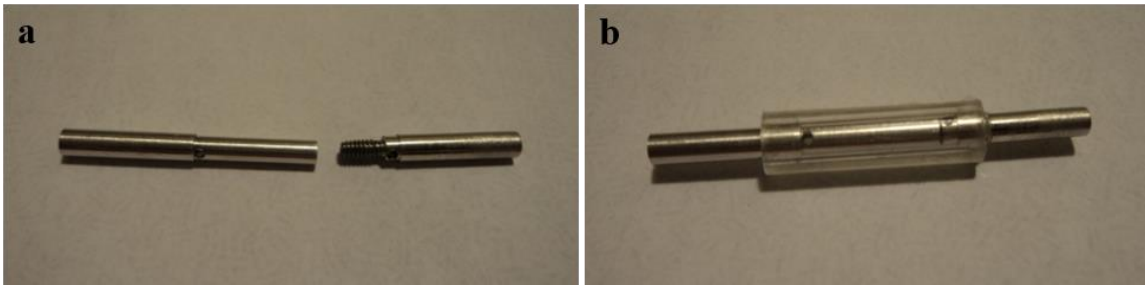

Figure 5.2: Mold to add phantom neointima coverage over the deployed stent: **a)** two pieces of the aluminum mold fasten together to provide a space between phantom vessel wall and outer surface of the mold to inject neointima material, **b)** mold placed inside a translucent phantom vessel.

Two pieces of the mold were inserted into phantom vessel from the two ends and a mix of PDMS and titanium dioxide was injected into the space between aluminum cylinder and vessel wall (Figure 5.3). After curing for 24 hours, the two halves of the aluminum cylinder were removed, leaving a phantom neointima covering the deployed stent.

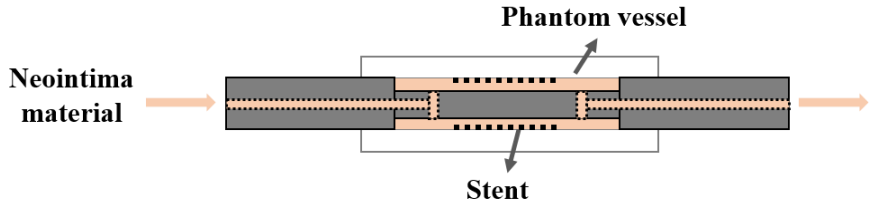

Figure 5.3: Addition of phantom neointima to the deployed stent inside phantom vessel.

ESTIMATING OPTICAL PROPERTIES OF NEOINTIMA

Optical properties of neointimal tissue, required for construction of phantom neointimas and optical simulations, have not been measured. As an approximation, properties of tissues with similar structures and reported values were utilized. Pathological observations of coronary stenting in humans have been reported in a few studies. Anderson et al. [47] reported presence of stent endothelialization and a thin neointima containing smooth muscle cells after 21 days. Komatsu et al. [48] showed actinpositive intimal smooth muscle cells 30 days after stenting. Van Beusekom et al. [49] reported leukocytes, platelets, and fibrin at three days and complete endothelial stent coverage and a smooth muscle cell-rich neointima after three months. Virmani et al. [50] published a comprehensive study on human coronary artery morphology early and late after stenting. Early after stenting (≤11 days) fibrin, platelets, and acute inflammatory cells (neutrophils) were nearly always present in association with stent struts (Figure 5.4-a). A well-defined neointima containing smooth muscle cells in a proteoglycan-collagen matrix and chronic inflammatory cells

(lymphocytes and macrophages) were recognized beginning about 2 weeks after stenting (Figure 5.4-b).

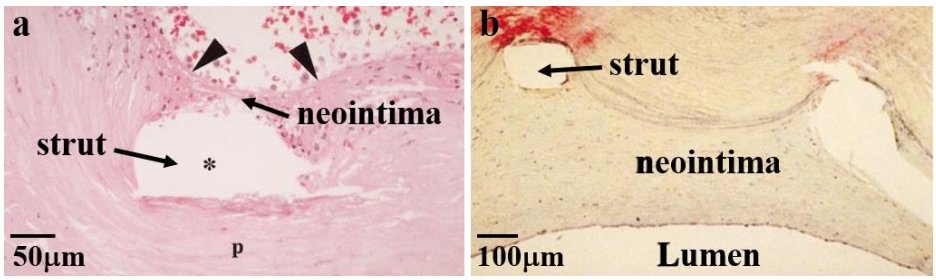

Figure 5.4: **a)** neonitimal formation after 3 days; fibrin, platelets, and acute inflammatory cells, **b)** neointimal formation after 120 days; smooth muscle cells, proteoglycan-collagen matrix, and chronic inflammatory cells [50].

Considering the cellular structure of neointimal layers, optical properties of human skin was selected where epidermis represents thin neonimas early after stenting and dermis represents thick neointimas in long term stenting. Reported scattering coefficients [51] and refractive indices [52] of epidermis and dermis at wavelength of 1310 nm are $\mu_s = 12.7$ cm^{-1} with $n = 1.42$ and $\mu_s = 8.1$ cm^{-1} with $n = 1.37$, respectively.

MICRO-CT IMAGES OF PHANTOM NEOINTIMA

Micro-CT imaging of phantom vessels with neointimal coverage were acquired applying the protocol described in section 3.1.5. When imaging the thin neointima, higher power was used to achieve a resolution of 3.5 μm (Figure 5.5).

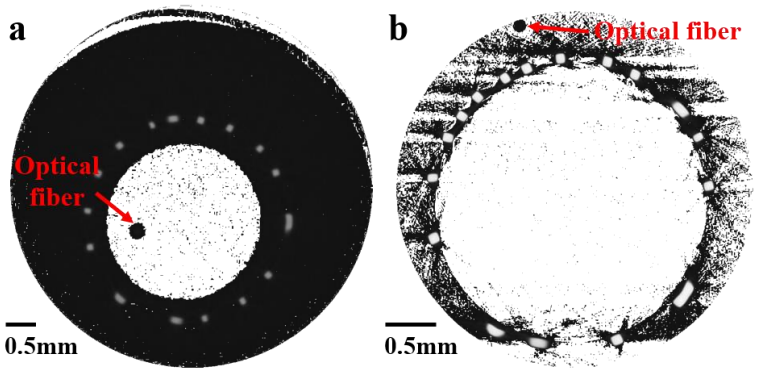

Figure 5.5: Micro-CT images of neointimal coverage over TAXUS® Liberte® stents; **a)** Micro-CT cross sectional image of thick neointima with resolution of 5.8 µm, **b)** Micro-CT cross sectional image of thin neointima with resolution of 3.5 µm. (negative images included for more visibility of phantom neointima layers)

IMAGE REGISTRATION

Image registration between IVOCT and Micro-CT data sets was performed in MATLAB (Mathworks, R2013a). Due to lower resolution, a single IVOCT frame corresponded to 7 Micro-CT sequential images of thick neointima and 18 sequential images of thin neointima. Therefore IVOCT frames were compared to superposition of Micro-CT images and a 125 µm diameter optical fiber oriented parallel to the long axis was embedded in the phantom vessel and used as marker.

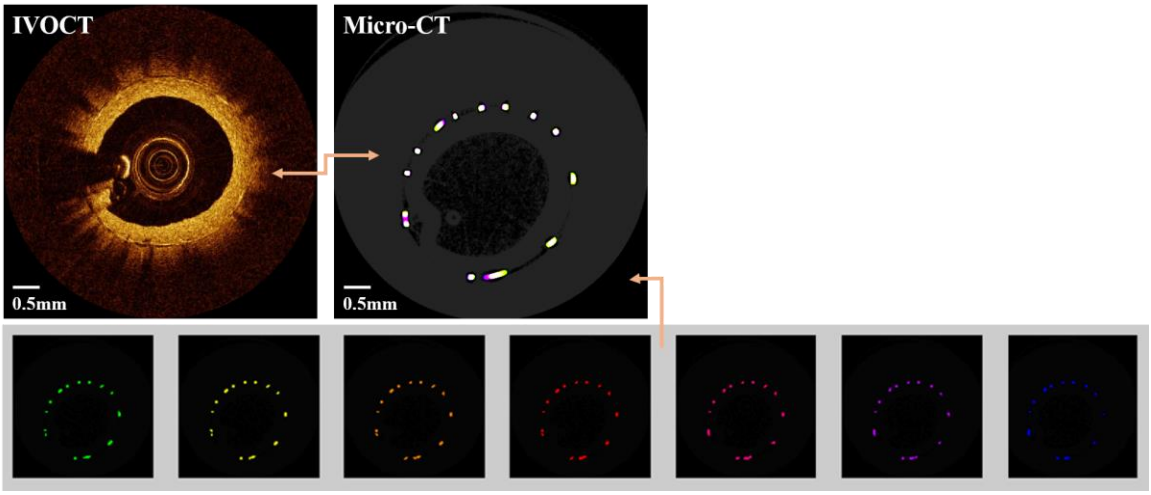

Figure 5.6: Image registration: an IVOCT frame (top left) and corresponding Micro-CT image (top right) obtained from superposition of 7 sequential images (bottom)

ACCURACY OF NEOINTIMAL THICKNESS MEASUREMENT

Measurements of neonitimal thickness from IVOCT images were compared to values obtained from Micro-CT images which represent actual neointimal thickness. Examples of thickness measurement for thick and thin neointimas are given in Figure 5.7 where we were able to measure the thickness of neointimal layers in IVOCT images as thin as 30 μm accurately. IVOCT and Micro-CT measurements of thicker neointima (Figure 5.7-a and b) match within 5 microns and in case of thin neointioma (Figure 5.7-c and d) there is a 2 microns error.

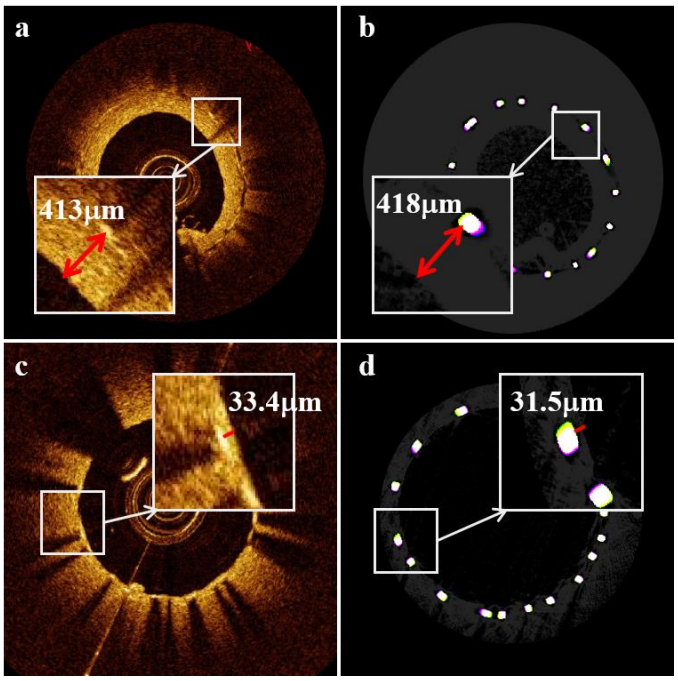

Figure 5.7: Neointimal thickness measurement; thick neointima by **a)** IVOCT and **b)** micro-CT and thin neointima by **c)** IVOCT and **d)** micro-CT.

Thickness measurement was done for several IVOCT images and the corresponding micro-CT images. To obtain physical lengths, measured *OPL*s were divided by refractive index of PDMS (1.405), instead of average refractive index of 1.33 used in Corevue system software when the lumen is flushed with saline. In addition, a correction was applied for non-normal incident light direction which makes a 16° angle with normal in air.

Measurements from 141 images of thick neointima are shown in Figure 5.8. Mean thickness measurement by IVOCT and micro-CT were 314.24 µm and 305.38 µm, respectively. Since micro-CT data is the gold standard, the fractional error in IVOCT measurements ($[mean_{IVOCT} - mean_{micro-CT}]/mean_{micro-CT}$) was 0.03. Measurement errors arise from user placement of the line segment and uncertainty in image registration caused by a slight catheter tilt.

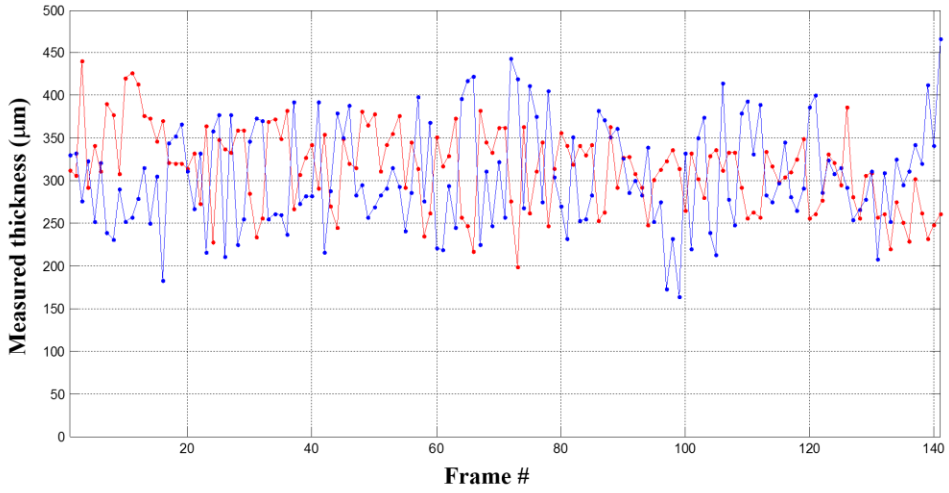

Figure 5.8: Measurement of thick neointima, red: IVOCT, blue: micro-CT.

Thin neointima measurement was done from 25 IVOCT images, since in some cases phantom tissue did not form over the entire stent. Results are shown in Figure 5.9 where mean thickness measurement by IVOCT and micro-CT were 48.47 μm and 38.22 μm, respectively and the fractional error in IVOCT measurements was 0.27. User placement of line segment results in larger errors when measuring thin neointimas, nonetheless an error of 10 μm is within the resolution of IVOCT.

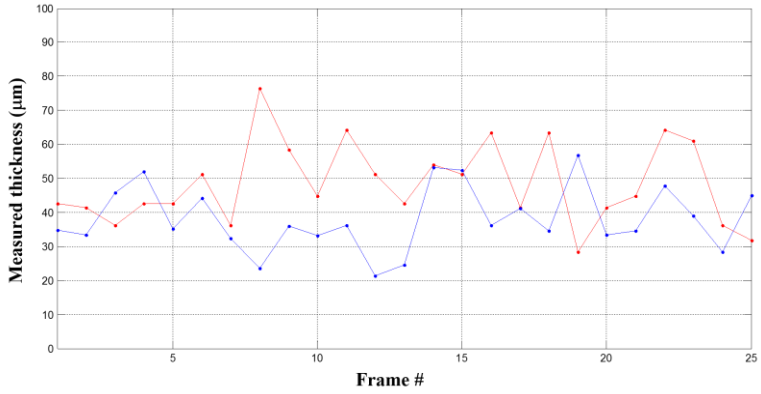

Figure 5.9: Measurement of thin neointima, red: IVOCT, blue: micro-CT.

EFFECTIVE LUMINAL SCATTERING

Residual blood

To study the effect of residual blood on detection of thin neointimal layers, goat blood was added to the saline at concentrations of 0.5, 1, 2 and 5%. IVOCT images of the stent with thin neointima coverage were acquired while the mix was injected by a syringe. As demonstrated in Figure 5.10 increasing the blood concentration increases luminal scattering, however, the presence of up to a 5% blood fraction does not affect the detection of thin neointimas.

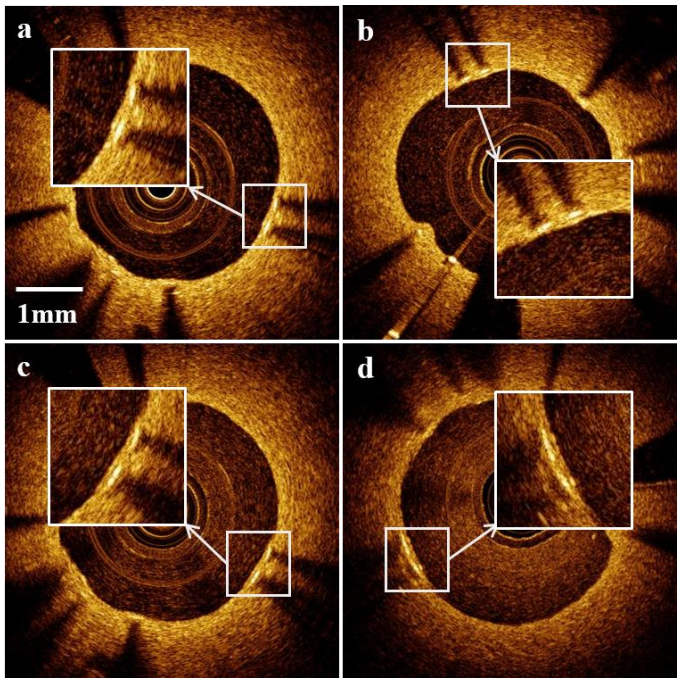

Figure 5.10: Effect of luminal scattering strength on detection of thin neointimas when flushed with: **a)** 0.5%, **b)** 1%, **c)** 2% and **d)** 5% blood volume fractions.

Power injector study

The scattering strength of flush fluid is unknown and measured with an OCT imaging system. A glass conduit with a rectangular cross section of 2×2 mm^2 was used for this experiment (Figure 5.11). A Medrad® Mark7 Arterion™ injector (Bayer Healthcare)

was utilized to power-inject contrast through a catheter to the glass conduit while the OCT signal amplitude was monitored from the back luminal surface of the glass conduit. Contrast was flushed at flow rates of 4, 5 and 6 ml/s at maximum pressure of 300 psi for 3 seconds while 300,000 A-scans were recorded at a fixed position. Measurement was repeated for glass conduit filled with contrast without flushing to obtain the background reference signal.

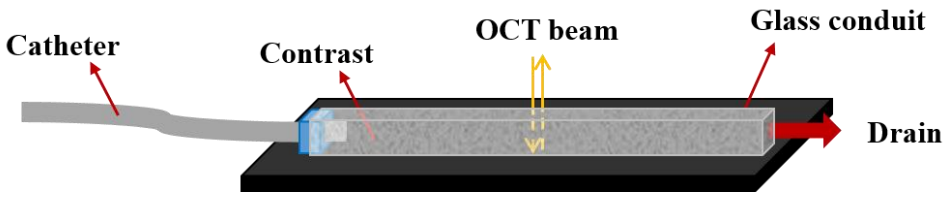

Figure 5.11: Experimental setup to study scattering strength of flush fluid

A-scans recorded during the middle second was used to ensure the beginning and end of flush did not affect the results. Signal intensity was averaged over every 100 A-scans and subtracted by the back ground signal. Figure 5.12 demonstrates the recorded signal (dB) over 1 second for different flow rates. The variation in signal intensity is not significant and increasing the flow rate did not have a noticeable effect. Consequently, scattering caused by flushing the contrast is negligible and will not affect IVOCT images.

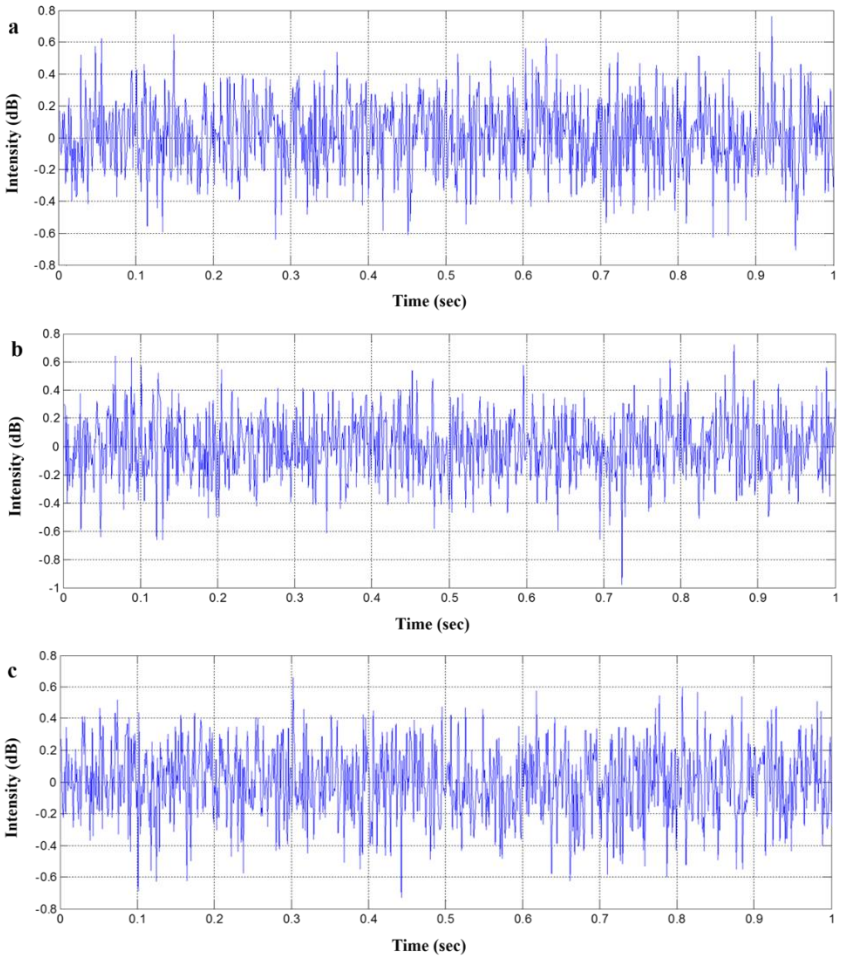

Figure 5.12: Intensity variation over 1sec for flow rates: **a)** 4 ml/sec, **b)** 5 ml/sec, and **c)** 6 ml/sec.

MERRY-GO-ROUND EFFECT DUE TO PRESENCE OF NEOINTIMA

Thicker neointimas may result in merry-go-rounding of stent struts in IVOCT images. Figure 5.13-c and d illustrate a selected strut covered by a neointimal thickness of 390 μm, while the measured length of the strut from the Micro-CT image is 199 μm, strut length measured from the corresponding IVOCT image is 275 μm. Thin neointima did not have an impact the apparent length of the strut in the IVOCT image (Figure 5.13-a and b).

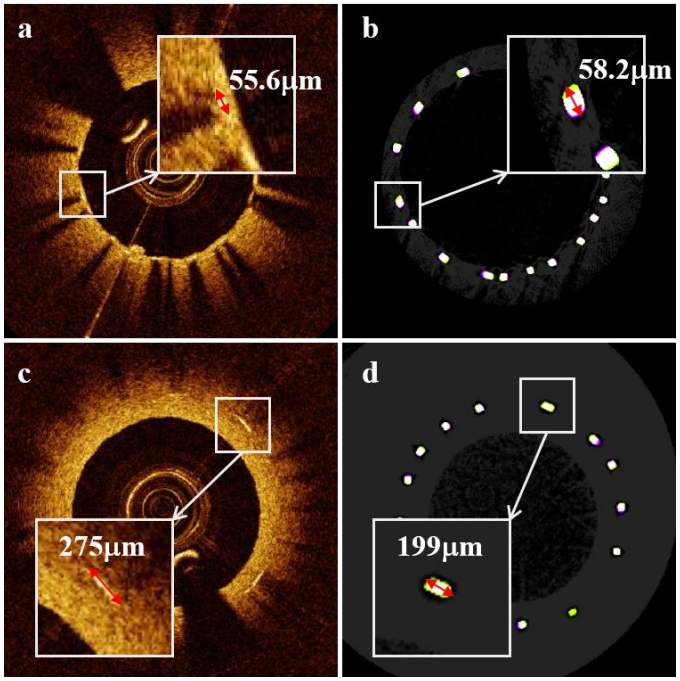

Figure 5.13: Effect of neointima on strut size; **a)** IVOCT and **b)** Micro-CT images of thin neointima, **c)** IVOCT and **d)** Micro-CT images of thick neointima where merry-go-round effect is observed.

The effect of neointimal coverage on the appearance of the strut is demonstrated in Figure 5.14. Increase in neointimal thickness results in stent strut elongation as reflected light is scattered inside the neointima and collected by neighboring A-scans. Since these signals do not correspond to the actual stent surface, no shadowing is observed behind elongated strut edges in thicker neointima.

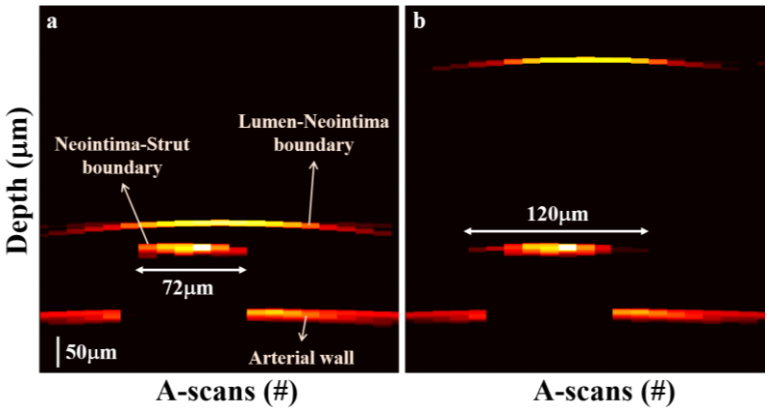

Figure 5.14: Simulated B-scans in presence of neointima: **a)** 50 μm thick, **b)** 400 μm thick

Optical simulations validate the mechanism of the merry-go-round effect; as neointimal layer becomes thicker, reflections from the strut surface undergo multiple scattering events and are collected by the IVOCT catheter. Therefore, struts in the IVOCT image appear elongated and the arterial wall is seen behind the artifactually formed edges while shadowing is confined to the mid portion of the strut.

SUNFLOWER WITH THICK NEOINTIMA

Effect of catheter eccentricity was studied by acquiring images at different catheter offsets at a fixed longitudinal position. In presence of a 200 micron thick neointima, sunflower effect was not observed. Measurements for four selected struts (Figure 5.15-a) showed catheter eccentricity does not impact neointima thickness measurements significantly (Table 5.1).

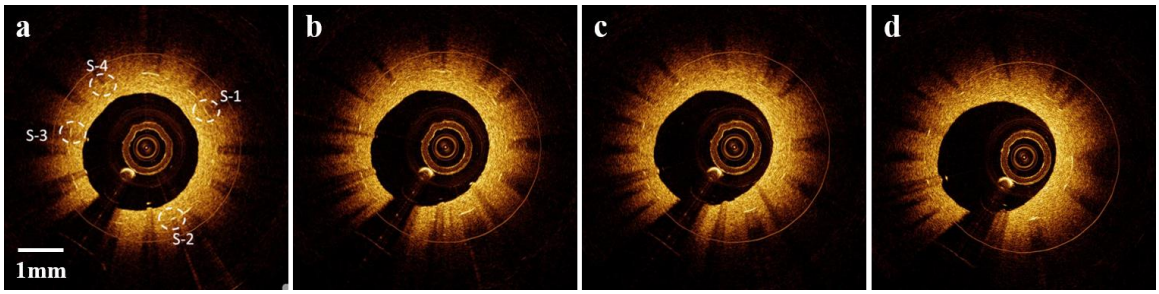

Figure 5.15: Sunflower effect is not observed in presence of thick neonitmas, catheter positions: **a)** P_1, **b)** P_2, **c)** P_3, and **d)** P_4.

Strut/Offset	P_1	P_2	P_3	P_4
S-1	223.81	225.23	304.10	229.81
S-2	194.54	194.97	196.26	192.10
S-3	176.40	181.66	185.69	179.89
S-4	209.52	213.27	214.67	207.51

Table 5.1: Effect of catheter eccentricity on neointima thickness measurements (μm)

The effect of neointimal coverage on the strut appearance in IVOCT images is demonstrated in Figure 5.14 in form of B-scans. Strut covered by neonitimal layer shown in Figure 3.10-c was assumed at four catheter eccentric positions (P_5-P_8) shown in Figure 3.10-b. Neointimal boundary appears at the top of the image with the underlying stent strut. The neointima becomes tilted as the catheter is placed at more eccentric positions while the strut appears oriented parallel to neointimal surface. Because neointimal surface roughness was not included in the model, weaker signals are observed at P_7 and P_8. Reflected light can undergo multiple scattering events inside neointima and therefore reflections from more regions on the strut are coupled into the catheter while the initial direction of reflections deviate from a specularly reflected incoming beam. As a result, in this circumstance sunflower effect does not occur and strut size and orientation are unaffected.

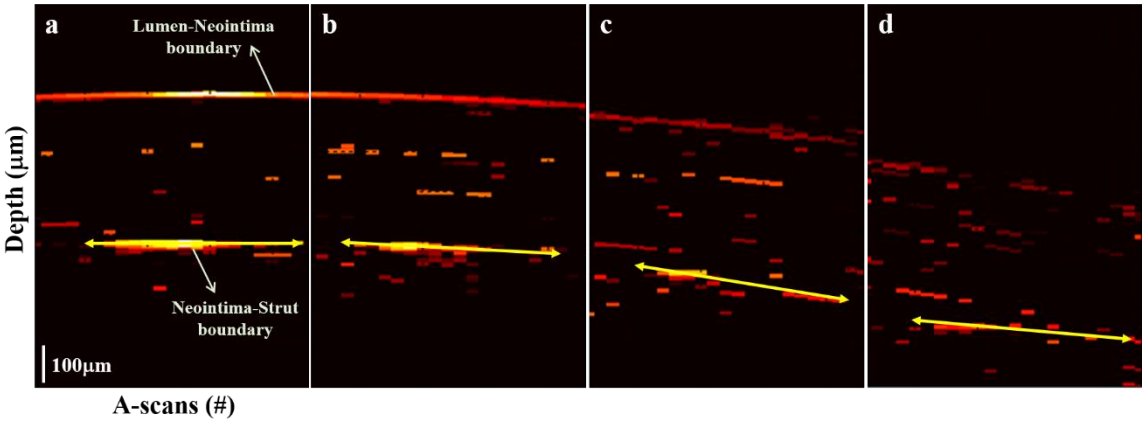

Figure 5.16: Strut size and orientation vs. catheter eccentricity in presence of thick neointima: **a)** P_5 (r_c = 0 mm), **b)** P_6 (r_c = 0.3 mm), **c)** P_7 (r_c = 0.6 mm), **d)** P_8 (r_c = 0.95 mm).

Chapter 6: Bioabsorbable stents

CURRENT STATUS OF BIOABSORBABLE STENTS

Metallic stents are permanent supports with a polymer coating eluting drug over two months. The need for vessel support and drug delivery is temporary and permanent support is unnecessary after the vessel has healed. Metallic stents in the long run may cause late stent thrombosis, expansive remodeling, side-branch obstruction by struts, difficulty in repeat surgical or percutaneous treatments and non-invasive imaging of coronary arteries with computed tomography or magnetic resonance [53-54].

Bioabsorbable drug-eluting stents are an alternative approach, providing short-term vessel scaffolding as well as drug delivery capability. After stent degradation, the vessel is returned to its natural functionality without a foreign body causing inflammation and less potential for late stent thrombosis [54-55]. The concerns with bioabsorbable stents include time and rate of degradation, biocompatibility, biodegradable products, elution of the drug, radial force and late recoil [55]. Degradation of a bioabsorbable stent should occur in a reasonable time period since stents must maintain their support strength for 6 months to reduce restenosis [56-58].

Tamai et al. [59] first examined the safety and feasibility of the bioabsorbable Igaki-Tamai stent (Igaki Medical Planning Co, Kyoto, Japan) in humans in 2000. Igaki-Tamai is a non-drug-eluting stent made of poly-L-lactic acid monofilament. The 6-month follow-up of all patients showed acceptable restenosis. Erbel et al. [60] reported the outcome of a bioabsorbable magnesium stent (BIOTRONIK, Berlin, Germany) in which stents safely degraded after 4 months. However, the recoil that was recorded with this stent resulted in a high restenosis rate, precluding further clinical use. Ormiston et al. [54] demonstrated the feasibility and safety of Absorb everolimus-eluting stent (Abbott Vascular, Santa Clara, CA). Absorb is made from a bioabsorbable poly-L-lactic acid which is coated with a more

rapidly absorbed poly-D,L-lactic acid layer that contains and controls the release of everolimus. Haude et al. [61] reported safety of a Drug (Paclitaxel) Eluting Absorbable Magnesium Scaffold (DREAMS). Results showed completion of the bioabsorption at 6 months with acute behavior that was comparable to conventional stents.

IVOCT IMAGES OF BIOABSORBABLE STENTS

In IVOCT images of bioabsorbable stents, struts appear as empty boxes where shadows are only seen along the two sides. Figure 6.1 illustrates IVOCT images of Absorb stent deployed in a phantom vessel recorded by a CoreVue system in our laboratory.

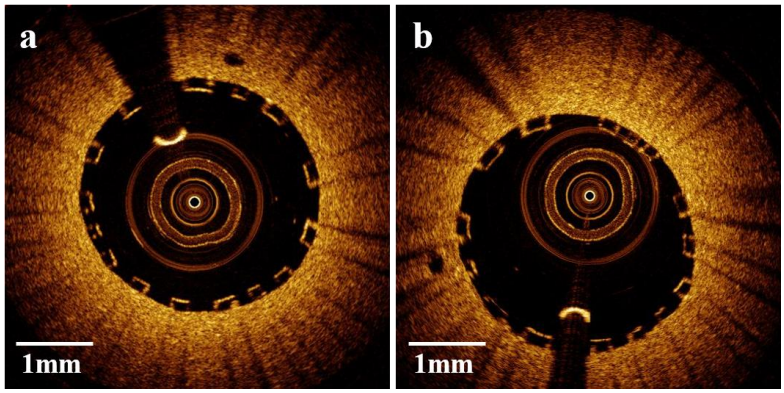

Figure 6.1: a) IVOCT image of a 3 mm Absorb coronary stent deployed in phantom vessel with centered catheter, **b)** IVOCT image of the phantom vessel with catheter adjacent to the luminal wall, orientation of struts is not affected by catheter eccentricity.

Stent struts do not always appear as a square or rectangular shape in IVOCT images which may be perceived as an imaging artifact. Micro-CT images of the Absorb stent (Figure 6.2) illustrates the actual shape of the struts where they are trapezoid and parallelogram shaped. Micro-CT images of the entire stent, also shows structure of bioabsorbable stent is not symmetric as compared to a metallic stent.

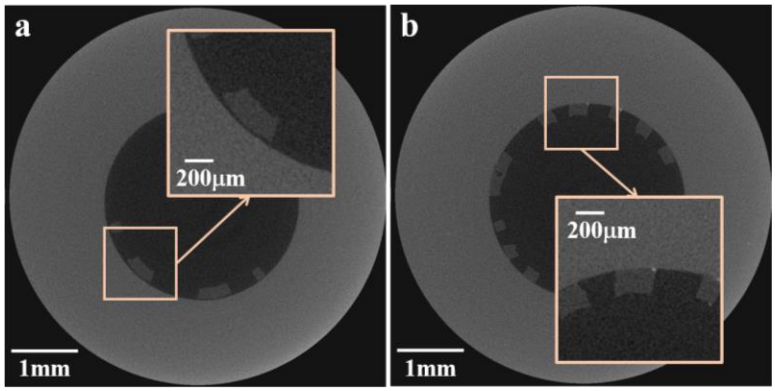

Figure 6.2: Micro-CT images of Absorb stent showing examples of **a)** a trapezoid shaped strut, **b)** a parallelogram shaped strut.

In some IVOCT images bright spots are observed inside the struts (Figure 6.3-a) that some hypothesized to be micro fractures formed in the structure of bioabsorbable stent due to stress possibly caused by tortuosity of the coronary arteries, the deployment or degradation process. However, micro-CT images of the Absorb stent (Figure 6.3-b) suggest that these bright spots correspond to the hollow spaces between the struts when they separate or merge together. These hollow spaces will act as strong scattering centers which would produce the bright spots observed inside the struts (Figure 6.3-a).

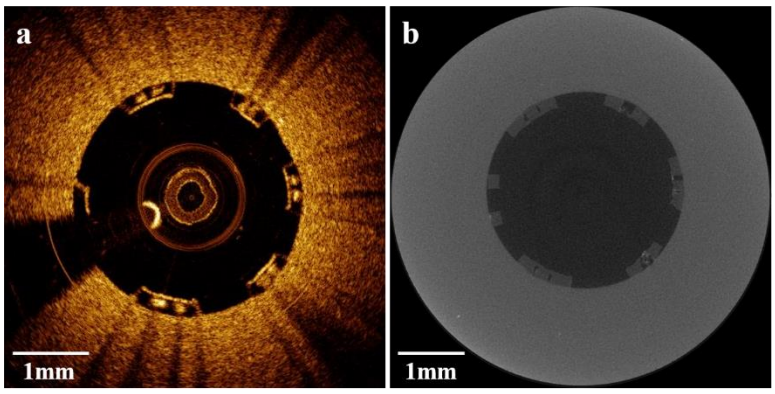

Figure 6.3: **a)** IVOCT image of a 3 mm Absorb coronary stent deployed in phantom vessel, **b)** Micro-CT image of the stent.

OPTICAL PROPERTIES OF STENT SURFACES

The distinct appearance of bioabsorbable stents in IVOCT images is due to optical properties of the strut surface. To examine the differences between metallic and bioabsorbale stents in IVOCT images, optical properties of the strut surfaces in a reflection model were characterized.

Surface reflection model

He et al. [62] described a light reflection model for an arbitrary medium in terms of bidirectional reflectivity ρ, consisting of three components:

$$\rho = \rho_{sp} + \rho_{dd} + \rho_{ud} \qquad (6.1)$$

where ρ_{sp}, ρ_{dd} and ρ_{ud} correspond to specular reflection, directional-diffuse and uniform-diffuse reflections, respectively. Figure 6.4 illustrates a general reflecting surface. The specular and directional-diffuse terms correspond to first-surface reflection while the uniform-diffuse corresponds to light that enters the medium, scatters and re-emerges.

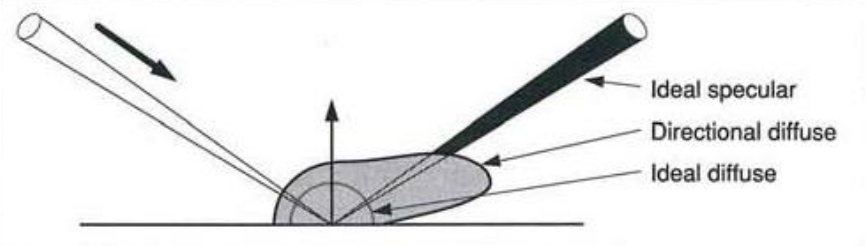

Figure 6.4: example of light intensity for a general reflecting surface [62]

Specular term accounts for mirror-like reflection from the mean plane of the reflecting surface:

$$\rho_{sp} \propto |F|^2 . e^{-g} = \rho'_{sp} \qquad (6.2)$$

where $|F|^2$ is the Fresnel's reflectivity and for a normally incident light is defined by refractive indices of the two media:

$$|F|^2 = \frac{(n_i - n_t)^2}{(n_i + n_t)^2} \qquad (6.3)$$

and g is a function of the surface roughness given by:

$$g = \left(\frac{4\pi\sigma}{\lambda}\right)^2 \qquad (6.4)$$

where σ is *rms* roughness of the surface and λ is the wavelength of incident light. Directional diffuse term corresponds to diffraction scattering by a rough surface:

$$\rho_{sp} \propto |F|^2 . \frac{\pi \tau^2}{4 \lambda^2} . \sum_{m=1}^{\infty} \frac{g^m e^{-g}}{m!\, m} e^{-\frac{4 \pi^2 \tau^2}{m \lambda^2}} = \rho'_{sp} \quad (6.5)$$

where τ is the autocorrelation length of the surface height variations. Uniform diffuse term is attributed to multiple surface and/or subsurface reflections, specified by Lambertian distribution and does not contribute to the surface features of bioabsorbable stents in IVOCT images.

Parameters required to characterize surface reflection properties include σ and τ which can be calculated directly from surface profile and refractive indices of the surface material and the surrounding medium. In this study, surface profiles of Cypher (metal) and Absorb (bioabsorbable) stents were obtained by atomic force microscopy at resolution of few nanometers to find σ and τ.

Determining surface parameters

Atomic force microscopy

Atomic force microscopy (AFM) is based on sensing the force on a sharp stylus created by the proximity to the surface of the sample. The interatomic forces induce the

displacement of the stylus, and in its original implementation, a tunneling junction was used to detect the motion of a diamond stylus attached to an electrically conductive cantilever beam [63]. Meyer and Amer [64] introduced an optical approach in which the cantilever displacement is measured by detecting the deflection of a weak laser beam which is reflected off its backside. Stylus which is located at the end of a lever made of material with extremely low stiffness is maintained in contact with the surface under very small loads - typically in the order of 1 nN [65]. The force F is measured by detecting the static deflection of the cantilever as its approaches the sample surface ($F = \Delta z\, k$ where Δz is the cantilever displacement from its equilibrium position and k is its force constant). As the tip is moved across the surface, a control feedback system constantly adjusts the tip to keep constant deflection. This adjustment represents the surface height variation.

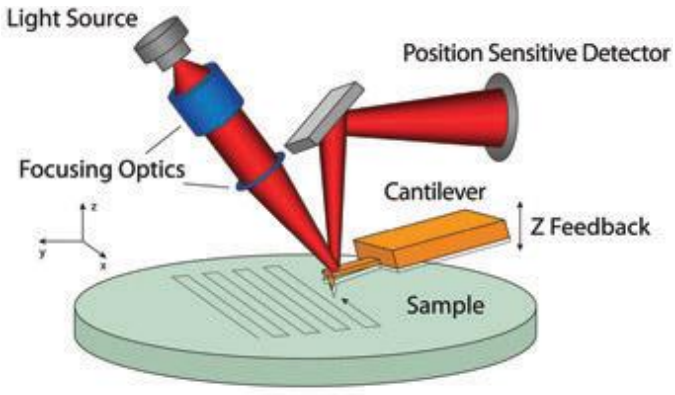

Figure 6.5: Schematic of AFM [66].

Stent surface profiles

Pieces of Absorb and Cypher stents strut were cut and secured on glass slides. A Pointprobe® (NANOSENSORS™, Neuchatel, Switzerland) with tip radius of less than 7 nm was used to scan the samples [67]. Surface areas of 10×10 μm^2 were scanned, acquiring

128×128 points which provided images with resolution of 78.12 nm. Figure 6.6 illustrates the measured variation in surface height of the two stent struts.

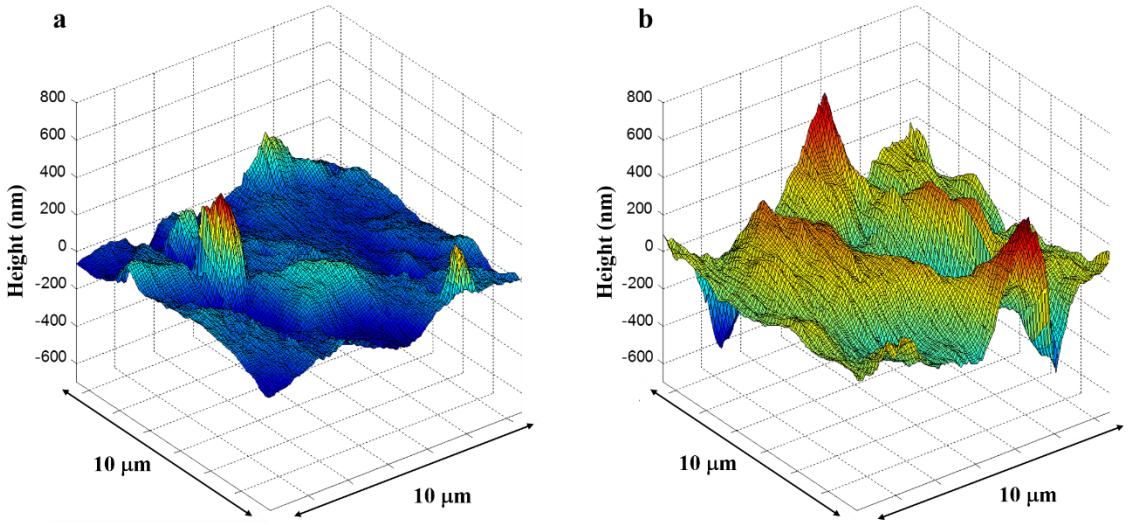

Figure 6.6: Surface profile: **a)** Absorb (bioabsorbable) and **b)** Cypher (metallic) stents.

Surface roughness found from AFM measured surface profiles of Absorb and Cypher were σ_a= 55.67 nm and σ_c= 123.79 nm, respectively. Auto correlation of the surface profiles was calculated and the full-width-half-maximum was measured. Correlation length of Absorb was τ_a= 1.17 μm. Auto correlation profile of Cypher was anisotropic and the mean of correlation lengths was assumed τ_c= 2.58 μm.

Refractive index measurement

Refractive index of Absorb was measured using an OCT system. A stent strut was secured on a glass slide and an OCT scan was recorded. Distance between the two reflections from air-polymer and polymer-air interfaces were taken as *OPL* and the distance from air-polymer to the reflection from glass slide was taken as the corresponding physical path length since the light traveled through air. Refractive index of Absorb was calculated by dividing *OPL* by the physical length which was 1.4.

Comparison of stent surface reflections

Specular and directional diffuse primed reflectivity of Absorb and Cypher stents were calculated using Eqs. 6.2 and 6.5. Fresnel reflection coefficient of Absorb was found using the measured refractive index n_a = 1.40 and assuming contrast flush for surrounding medium (n_a = 1.45), giving $|F|^2$ = 3.7×10^{-4}. Cypher stent is composed of stainless steel with reported refractive index of $n = 4.1 + 5.8i$ [68]. Computed Fresnel reflectivity for normal incidence is $|F|^2$ = 0.79. Specular (ρ'_{sp}) and directional diffuse (ρ'_{dd}) primed reflectivity of Cypher and Absorb stents are given in Table 6.1

	$\boldsymbol{\rho'_{sp}}$	$\boldsymbol{\rho'_{dd}}$
Cypher	0.19	5.53×10^{-13}
Absorb	2.78×10^{-4}	1.24×10^{-11}

Table 6.1: Specular (ρ'_{sp}) and directional diffuse (ρ'_{dd}) primed reflectivities of Cypher and Absorb stents.

Magnitude of the primed reflectivity does not directly give the magnitude of the reflected light without accounting for the incident and reflected solid angles, nonetheless, relative values of primed reflectivity provide a basis to describe the appearance of the Absorb and Cypher stents in IVOCT images. Specular primed reflectivity of Cypher is almost three orders of magnitude larger than the Absorb, and therefore, strong specular reflections from metal stent surfaces are recorded which are dependent on the direction of incident beam. IVOCT images of metallic stents do not normally show specular reflection of the strut sides since the surface normal does not match the direction of incoming light. Relative magnitude of directional diffuse to specular primed reflectivity is much larger for Absorb which is consistent with observations of Absorb struts where light backscattered from the strut sides is observed. The relative contribution of the directional diffuse component to observed strut surfaces in IVOCT images is larger for the Absorb compared

to Cypher. Since the IVOCT beam orientation does not affect the appearance of struts, sunflower artifact is not observed when the catheter is at eccentric positions. Additionally, no reflection is recorded at depths corresponding to the inside of the struts due to optical homogeneity of the polymer comprising the strut. This allows the reflection at arterial wall boundary to be recorded and shadows only form along the two sides of the struts.

Chapter 7: Metal Stent Artifact Correction Algorithm

ALGORITHM OUTLINE

The objective of these studies is to develop an algorithm to replace the apparent struts rendered from IVOCT images of a metallic stent recorded from one pullback with the actual stent structure based on Micro-CT imaging.

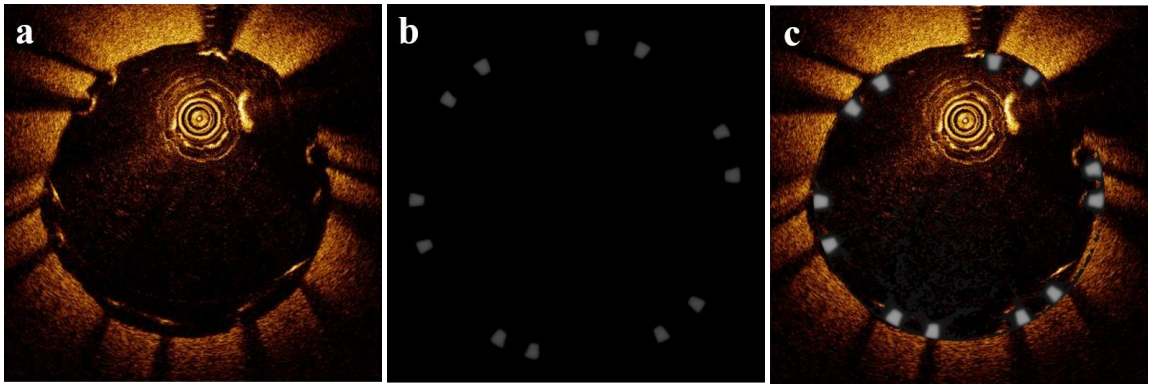

Figure 7.1: Approach for artifact construction algorithm. **a)** IVOCT image of CYPHER® stent deployed in a phantom vessel demonstrating sunflower and merry-go-round artifacts, **b)** CYPHER® stent imaged by Micro-CT, **c)** Corrected IVOCT image with artifacts removed.

The stent size and orientation as recorded by Micro-CT and recorded IVOCT images are utilized to correct for strut artifacts. A flow diagram of the proposed algorithm is demonstrated in Figure 7.2.

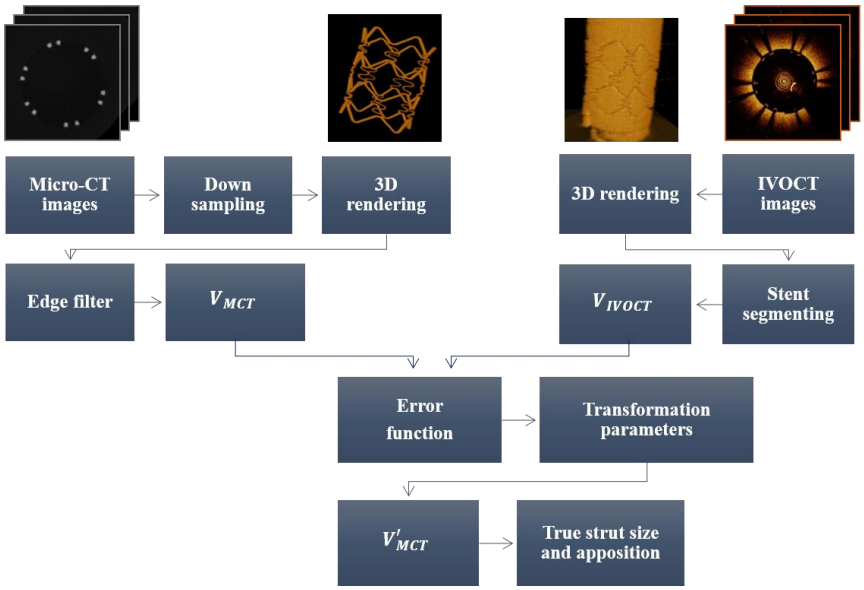

Figure 7.2: Block diagram of the correction algorithm; top left: Micro-CT data is processed by first down sampling, rendering in three-dimensions, applying an edge filter and deriving dataset v_{MCT}, top right: IVOCT images of a pullback are rendered and struts are segmented, obtaining dataset v_{IVOCT}, bottom: an error function is minimized by iteratively changing transformation parameters which are applied to v_{MCT}. The best overlap achieved by v'_{MCT} gives an artifact-free image of strut size and apposition.

Micro-CT images are rendered and must first be down-sampled since their voxel size is about 10-fold finer than that of IVOCT images. After down sampling, an edge filter is applied to stent struts in the Micro-CT image to find the inner surface of struts and x, y and z coordinate locations and surface normals of the selected points for storage in V_{MCT}. IVOCT images of a pullback are rendered and apparent struts in a deployed stent are obtained using image segmentation, giving a three-dimensional representation of the apparent stent struts and x, y and z coordinate locations be will stored in V_{IVOCT}. Objective of the algorithm is to determine the values of the transformation parameters that provide the best overlap between V_{IVOCT} and V_{MCT}. The transformation parameters are determined by minimizing an error function (Eq. 7.1).

$$Erorr\ (p) = \sum_{i,j,k}(V_{IVOCT} - V_{MCT}(p))^2 \qquad (7.1)$$

where p is an array of transformation parameters. Having found the parameters, Micro-CT data set is transformed and inserted into the IVOCT image to give an artifact-free image of strut size and apposition.

STENT DATABASE

Micro-CT images of a CYPHER® stent were used to reconstruct a three-dimensional representation of the whole strut which was stored in a stereolithography (STL) file format. STL files define geometry of an object by breaking down the surface into triangles, also called facets (Figure 7.3). Each facet is described by coordinate locations of the three vertices and direction of the surface normal.

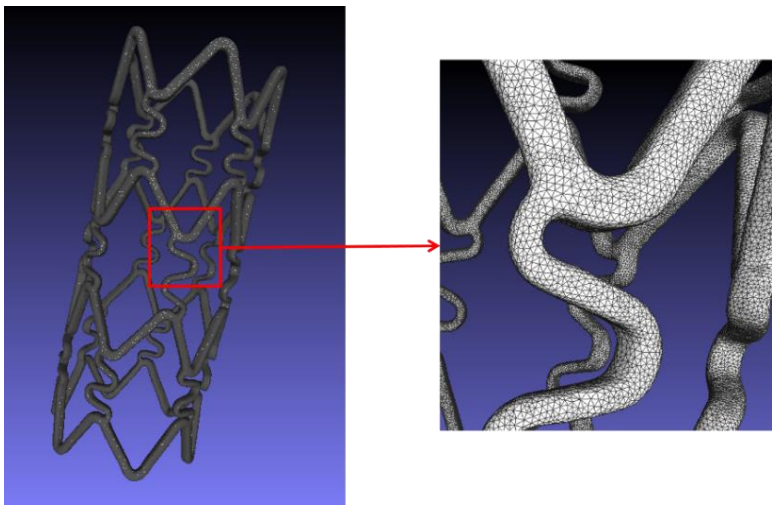

Figure 7.3: Three dimensional model of CYPHER® stent stored in STL file, close up: triangles defining the stent surface.

Using a reader [69], STL file data was imported into MATLAB by creating three matrices shown in Figure 7.4:

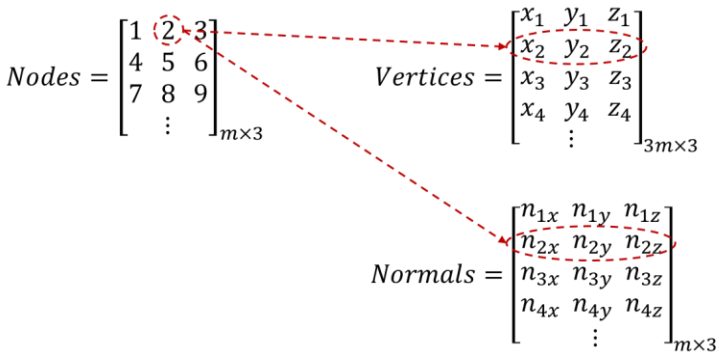

Figure 7.4: Reading an STL file in MATLAB. Number of triangles is denoted by m. In the Nodes matrix, the m'th row represents the vertices of the m'th triangle. Each row in the Vertices matrix represents coordinates (x,y,z) of one vertex. The m'th row of the Normals matrix represents the unit normal to the m'th triangle.

Node numbers of each triangle is listed in one row of matrix Nodes, where m is the total number of triangles, *(x,y,z)* coordinates of each node can be found in the Vertices matrix. The m'th row of the vertices number is equivalent to the node number. The surface normal of each triangle is stored in matrix Normals, at a row number equivalent to the triangle number. Vertices coordinate locations of each triangle were averaged and stored in an m×3 array as stent position data S_p and the corresponding surface normal was stored as the stent normal data S_n. When imaging a deployed stent within an artery, IVOCT catheter only collects reflections from the inner surface of the stent. Consequently, positions and normals of triangles forming the outer surface of the stent were omitted from stent database (Figure 7.5).

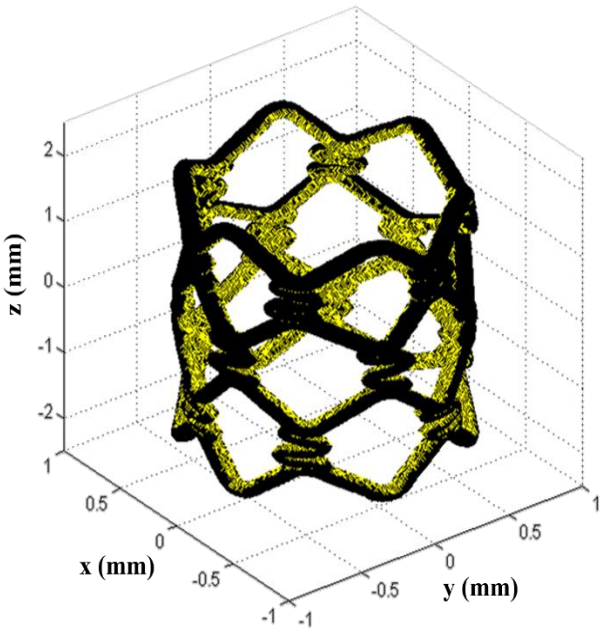

Figure 7.5: Imported CYPHER® stent positions into MATLAB, selected inner surface for simulating pullback are shown in yellow.

GLOBAL COORDINATE SYSTEM FOR STENT DATABASE

Stent database obtained from STL file is taken as the global coordinate system in which the pullback is simulated. Stent orientation and center of mass, shown in Figure 7.6 were used for coordinate transformation.

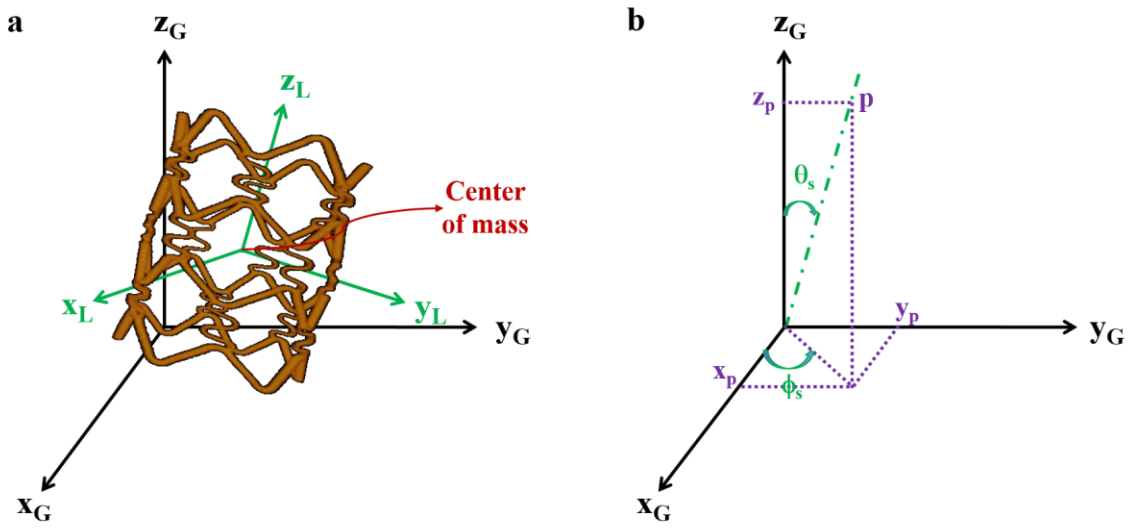

Figure 7.6: **a)** Stent orientation (φ_s and θ_s) and center of mass (p_{cm}) in global coordinate system (black axes), simulated pullback is generated in local coordinate system (green axes) and transformed to global coordinate system using φ_s, θ_s and p_{cm}, **b)** finding φ_s and θ_s values.

Center of mass (p_{cm}) was calculated by Eq.7.2 and utilized to translate the local coordinate system along x and y axes. The z axis was translated by $(z_{cm} - z_{min})$ where z_{min} was the minimum z coordinate of stent database that has only positive z values.

$$x_{cm} = (\sum_{i=1}^{m} x_i)/m \ , \ y_{cm} = (\sum_{i=1}^{m} y_i)/m \ , \ z_{cm} = (\sum_{i=1}^{m} z_i)/m \qquad (7.2)$$

Stent orientation was described by two angles φ_s, representing a rotation about z axis and θ_s, a rotation about x axis which were calculated by taking a point (p) on the z axis of local coordinate system and finding the corresponding coordinate location in global coordinate system:

$$\varphi_s = \tan^{-1} y_p/x_p \qquad (7.3)$$

$$\theta_s = \tan^{-1} \sqrt{{x_p}^2 + {y_p}^2}/z_p \qquad (7.4)$$

where x_p, y_p, and $z_p$the coordinate locations of p in global coordinate sysyem.

LOCAL TO GLOBAL COORDINATE TRANSFORMATION

Local coordinate system in which a helix function is generated is transformed to the global coordinate system. The helix function represents angular orientation of the light beam exiting the IVOCT catheter. Transformation parameters include a translation by the stent center of mass and Euler angle rotations to account for the stent orientation.

Euler's angles

Euler angles, typically denoted by φ, θ, ψ are used to represent the orientation of a coordinate system relative to another. Euler angles correspond to a sequence of three rotations about the axes of a coordinate system, starting from a known standard orientation (Figure 7.7). Any rotation matrix R can be decomposed as a product of three elemental rotation matrices A, B and C given by Eq.6.5 and 6:

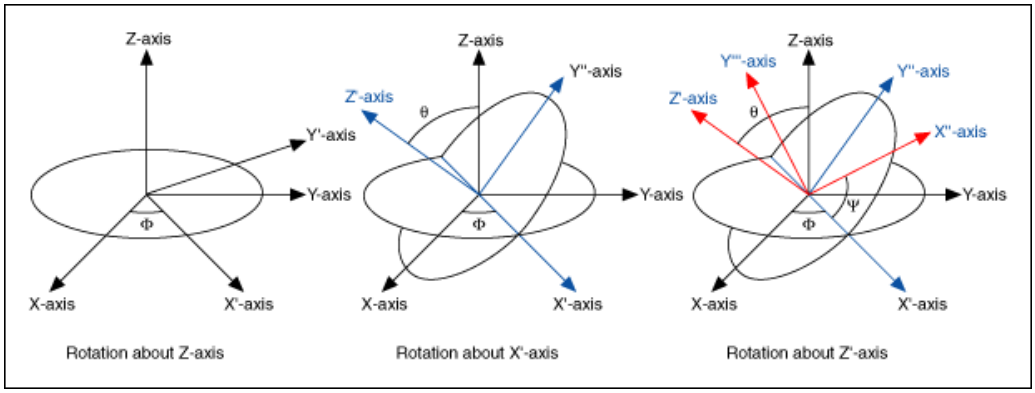

Figure 7.7: Coordinate rotation with the Euler angles φ, θ, ψ [70]

$$C = \begin{bmatrix} cos\,\varphi & sin\,\varphi & 0 \\ -sin\,\varphi & cos\,\varphi & 0 \\ 0 & 0 & 1 \end{bmatrix}, \quad B = \begin{bmatrix} 1 & 0 & 0 \\ 0 & cos\,\theta & sin\,\theta \\ 0 & -sin\,\theta & cos\,\theta \end{bmatrix}, \quad A = \begin{bmatrix} cos\,\psi & sin\,\psi & 0 \\ -sin\,\psi & cos\,\psi & 0 \\ 0 & 0 & 1 \end{bmatrix} \tag{7.5}$$

$$R = ABC \qquad (7.6)$$

$$= \begin{bmatrix} cos\,\psi\,cos\,\varphi - cos\,\theta\,sin\,\varphi\,sin\,\psi & cos\,\psi\,sin\,\varphi + cos\,\theta\,cos\,\varphi\,sin\,\psi & sin\,\psi\,sin\,\theta \\ -sin\,\psi\,cos\,\varphi - cos\,\theta\,sin\,\varphi\,cos\,\psi & -sin\,\psi\,sin\,\varphi + cos\,\theta\,cos\,\varphi\,cos\,\psi & cos\,\psi\,sin\,\theta \\ sin\,\theta\,sin\,\varphi & -sin\,\theta\,cos\,\varphi & cos\,\theta \end{bmatrix}$$

DEFINING HELIX

Functions describing coordinates of a circular helix H_p with radius r and the normals H_n are defined by

$$H_p(t) = \begin{bmatrix} r\,cos\,\varphi \\ r\,sin\,\varphi \\ c\,t \end{bmatrix} \qquad (7.7)$$

$$H_n(t) = \begin{bmatrix} -cos\,\varphi \\ -sin\,\varphi \\ 0 \end{bmatrix} \qquad (7.8)$$

$$\varphi = 2\pi f t \qquad (7.9)$$

where φ is the phase, f is catheter rotation speed (rpm), t is pullback time (s), c is the pullback speed (mm/s). To simulate the effect of catheter position and orientation and the position of the starting A-scan on the generated pullback, H_p and H_n functions are modified by introducing variables that correspond to each effect; the position of the first A-scan is given by z_p and φ_p causing an offset along the catheter and a phase offset, respectively

$$H_p(t) = \begin{bmatrix} r\,cos(\varphi + \varphi_p) \\ r\,sin(\varphi + \varphi_p) \\ c\,t + z_p \end{bmatrix} \qquad (7.10)$$

$$H_n(t) = \begin{bmatrix} -cos(\varphi + \varphi_p) \\ -sin(\varphi + \varphi_p) \\ 0 \end{bmatrix} \qquad (7.11)$$

catheter position is given by x_c and y_c from the center results in a translation in the helix function

$$H_p(t) = \begin{bmatrix} r\,cos(\varphi + \varphi_p) + x_c \\ r\,sin(\varphi + \varphi_p) + y_c \\ c\,t + z_p \end{bmatrix} \qquad (7.12)$$

and catheter orientation defined by two angles φ_c and θ_c (assuming $\psi_c = 0$) results in a coordinate rotation which can be described using Euler's angles (Eq.7.6), multiplying $H_p(t)$ and $H_n(t)$ by rotation matrix R_c the modified helix considering all variables is obtained

$$\widehat{H}_p(t) = \begin{bmatrix} cos\,\varphi_c\,[\,r\,cos(\varphi + \varphi_p) + x_c] + sin\,\varphi_c\,[\,r\,sin(\varphi + \varphi_p) + y_c] \\ -cos\,\theta_c\,sin\,\varphi_c\,[\,r\,cos(\varphi + \varphi_p) + x_c] + cos\,\theta_c\,cos\,\varphi_c\,[\,r\,sin(\varphi + \varphi_p) + y_c] + sin\,\theta_c\,(c\,t + z_p) \\ sin\,\theta_c\,sin\,\varphi_c\,[\,r\,cos(\varphi + \varphi_p) + x_c] - sin\,\theta_c\,cos\,\varphi_c\,[\,r\,sin(\varphi + \varphi_p) + y_c] + cos\,\theta_c\,(c\,t + z_p) \end{bmatrix}$$

(7.13)

$$\widehat{H}_n(t) = \begin{bmatrix} -cos\,\varphi_c\,cos(\varphi + \varphi_p) - sin\,\varphi_c\,sin(\varphi + \varphi_p) \\ cos\,\theta_c\,sin\,\varphi_c\,cos(\varphi + \varphi_p) - cos\,\theta_c\,cos\,\varphi_c\,sin(\varphi + \varphi_p) \\ -sin\,\theta_c\,sin\,\varphi_c\,cos(\varphi + \varphi_p) + sin\,\theta_c\,cos\,\varphi_c\,cos(\varphi + \varphi_p) \end{bmatrix} \qquad (7.14)$$

SIMULATED PULLBACK

Generated helix positions and normals based on given parameters were utilized to simulate a pullback from the stent dataset. To find the reflecting region of the stent that is recorded by each A-scan, first the stent regions whose normals' direction is within an accepted angular tolerance of the A-scan's normal are determined first. This was done by calculating the dot product of the A-scan's direction with all the stent normals which gives the angle between two directions since their magnitudes are one (Eq.7.15). The accepted angular tolerance represents change in wavefront normal for the OCT light assumed to be a Gaussian beam.

$$S_n . H_n = |S_n||H_n|\,cos\,\theta < cos(\pi - \alpha) \qquad (7.15)$$

where H_n is the helix normal, S_n is the stent normal, θ is the angle between the normals, and α is the accepted angular tolerance. As multiple helix positions with equivalent normals exist, not all stent positions whose normal meet this condition correspond to the helix position. Therefore, only the positions that are within in an accepted distance from the intersection of A-scan and stent. Figure 7.8 illustrates the generated helix, stent and a selected A-scan represented by a helix position $H_{p,i}$ and surface normal $H_{n,i}$.

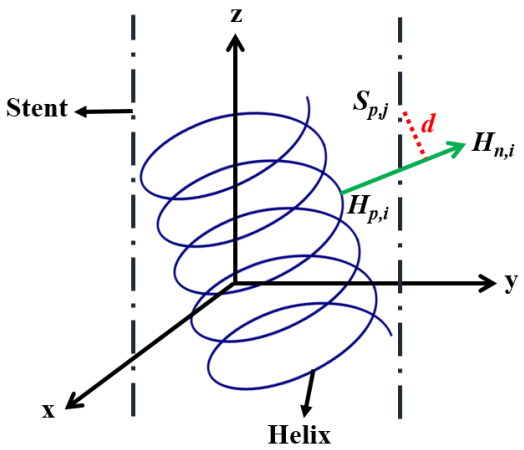

Figure 7.8: Simulated pullback; a selected A-scan is indicated by helix position $H_{p,i}$ and surface normal $H_{n,i}$, accepted stent position $S_{p,j}$ within distance d from $H_{n,i}$.

Distance, denoted by d, is defined and constrained by

$$d = \left|(S_p - H_p) - [(S_p - H_p).H_n]H_n\right| < \beta \qquad (7.16)$$

where S_p is the stent position, H_p is the helix position, H_n is the helix normal, and β is the accepted distance range. The accepted distance represents spot-size of the Gaussian beam that was approximated as a constant.

Stent positions that meet the criteria in Eqs. 7.15 and 7.16 are included in the simulated pullback data. Depending the catheter parameters, number of selected points on

the stent could vary. To keep the size of simulated pullback constant, an array ($\hat{y}$) was defined for the output B-scan data. The index of the $\hat{y}$ array corresponds to the A-scan # while the value in the array corresponds to distance of the strut (if present) from the catheter. If no strut is present for a particular A-scan then a value of zero is assigned at that index (Figure 7.9).

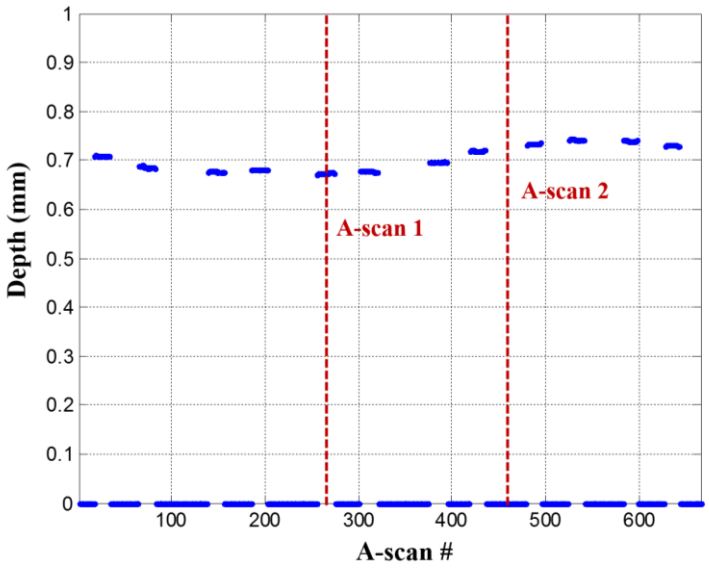

Figure 7.9: Selected subset of simulated B-scan ($\hat{y}$); in A-scan 1 (#265) light was reflected and depth of strut 0.67 mm was stored, in A-scan 2 (#458) no stent positions were found from which light was reflected and therefore a zero was assigned.

OBJECTIVE FUNCTION

The objective function to be fitted to an IVOCT pullback was defined in Matlab as follows:

- Pullback data (catheter rotation frequency (f), pullback speed (c) and pullback duration (t). are provided to generate the helix function.
- Catheter position (x_c and y_c), catheter orientation (φ_c and θ_c) and position of first A-scan (z_p and φ_p) are used to modify the helix in the local coordinate system.

- Helix function is transformed to the global coordinate system using stent center of mass (x_{cm}, y_{cm}, and z_{cm}) and stent orientation (φ_s and θ_s).
- Pullback is simulated using the Helix function and stored stent database.

Figure 7.10 illustrates two examples of a simulated pullback where all parameters are assumed 0 (top) and where parameters are x_c = 0.05, y_c = 0.05, φ_c = π/8, θ_c = π/15, z_p = 0.1, and φ_p = π/4 (bottom).

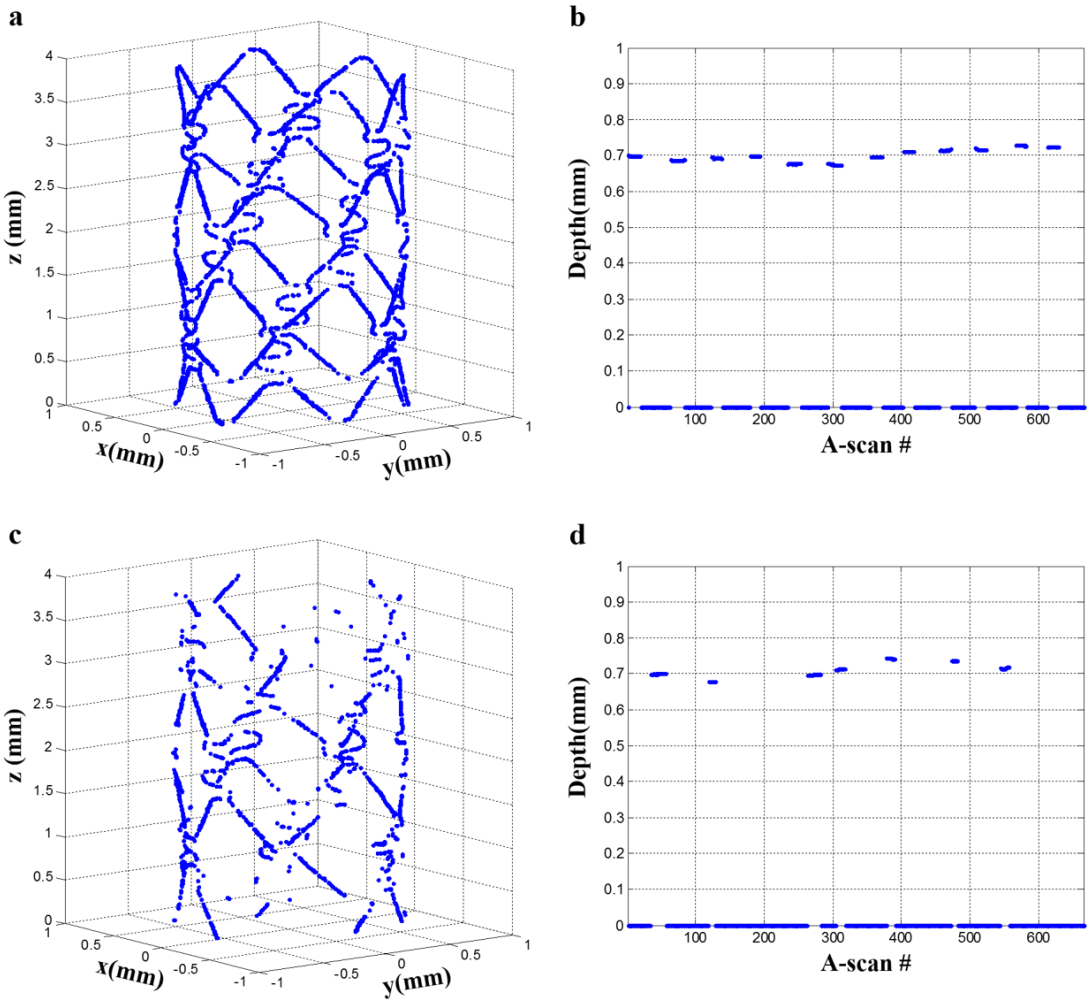

Figure 7.10: Examples of two simulated pullbacks: **a)** 3D representation of pullback 1 where all parameters (x_c, y_c, φ_c, θ_c, z_p, and φ_p) are zero, **b)** a selected simulated B-scan ($\hat{y}$), **c)** 3D representation of pullback 2 with parameters x_c = 0.05, y_c = 0.05, φ_c = π/8, θ_c = π/15, z_p = 0.1, and φ_p = π/4, **d)** selected simulated B-scan corresponding to selected B-scan in **b**.

LEVENBERG-MARQUARDT ALGORITHM

The Levenberg-Marquardt algorithm is a standard technique used to solve nonlinear optimization problems which involve an iterative improvement to parameter values in order to reduce the sum of the squares of the errors between an objective function

and the measured data points [71-72]. Assuming data points are denoted by $y = (y_1, y_2, \dots, y_n)$ and the model to be fitted is given by $\hat{y} = f(x_1, x_2, \dots, x_n, p_1, p_2, \dots, p_m)$, where x_i is i[th] independent variable and p_i is the i[th] parameter, the objective is to compute estimates of the parameters which will minimize $\sum|y - \hat{y}|^2$. The scalar-valued goodness-of-fit measure is called the chi-squared error criterion given by

$$\chi^2(p) = \frac{1}{2}\sum_{i=1}^{m}\left[\frac{y_i - \hat{y}(x_i, p)}{w_i}\right]^2$$

$$= \frac{1}{2}\big(y - \hat{y}(p)\big)^T W(y - \hat{y}(p)) \qquad (7.17)$$

where w_i is a measure of the error in measurement y_i and weighting matrix W is diagonal with $W_{ii} = 1/w_i^2$ [71]. Since function $\hat{y}$ is nonlinear in the model parameters p, the minimization of χ^2 must be carried out iteratively, by applying a perturbation h to the parameters at each iteration.

The Levenberg-Marquardt algorithm is a combination of two minimization methods: the steepest gradient descent and the Gauss-Newton method. The algorithm behaves like a steepest descent method when the parameters are far from the optimal values and it becomes a Gauss-Newton method when parameters are close to the optimal values [73].

Steepest gradient descent Method

The steepest gradient descent is a general minimization method which updates parameter values in the direction opposite to the gradient of the objective function. It is recognized as a highly convergent algorithm for finding the minimum of simple objective functions [72, 74]. The gradient of the chi-squared objective function with respect to the parameters is given by

$$\frac{\varrho}{\varrho p}\chi^2(p) = \left(y - \hat{y}(p)\right)^T W \frac{\varrho}{\varrho p}\left(y - \hat{y}(p)\right)$$

$$= -\left(y - \hat{y}(p)\right)^T W \left[\frac{\varrho \hat{y}(p)}{\varrho p}\right] \qquad (7.18)$$

where $[\varrho\hat{y}(p)/\varrho p]$ represents the local sensitivity of $\hat{y}$ variation in the parameters, also called Jacobian matrix (J). The perturbation h that moves the parameters in the direction of steepest descent is given by

$$h_g = \alpha J^T W(y - \hat{y}) \qquad (7.19)$$

where the positive scalar α determines the length of the step in the steepest-descent direction.

The Gauss-Newton Method

The Gauss-Newton method is a method of minimizing a sum-of-squares objective function. Objective function is assumed quadratic in the parameters near the optimal solution. The function evaluated with perturbed model parameters may be approximated by first-order Taylor series expansion:

$$\hat{y}(p + h) \approx \hat{y}(p) + \left[\frac{\varrho \hat{y}}{\varrho p}\right] = \hat{y} + Jh \qquad (7.20)$$

The perturbation h that minimizes χ^2 is found by $\varrho\chi^2/\varrho h$=0 where $\hat{y}$ in Eq.6.17 is substituted by approximation for the perturbed function, $\hat{y} + Jh$ and the resulting normal equations for the Gauss-Newton perturbation are

$$[J^T W J]h_{gn} = J^T W(y - \hat{y}) \qquad (7.21)$$

Levenberg-Marquardt method as a blend of steepest gradient descent and Gauss-Newton method

The Levenberg-Marquardt algorithm varies the parameter updates between the steepest gradient descent and Gauss-Newton update:

$$[J^T W J + \lambda I] h_{lm} = J^T W (y - \hat{y}) \qquad (7.22)$$

where small values of the algorithmic parameter λ result in a Gauss-Newton update and large values of λ result in a steepest gradient descent update. At a large distance from the function minimum, the steepest gradient descent method is utilized to provide steady and convergent progress toward the solution. As the solution approaches the minimum, λ is adaptively decreased and the Levenberg-Marquardt method approaches the Gauss-Newton method, and the solution typically converges rapidly to the local minimum [72-74].

IMPLEMENTING LEVENBERG-MARQUARDT ALGORITHM

Matlab optimization toolbox (lsqcurvefit function) was utilized to apply the Levenberg-Marquardt algorithm. The objective function ($\hat{y}$), independent variables (x), initial parameters (p_o) and the data (y) are specified, lsqcurvefit starts at p_o and finds parameters p to best fit the nonlinear objective function $\hat{y} = f(x, p)$ to the data y [75]. The objective function of this study does not take independent variables (x) as input, only parameters (p) are needed to generate a simulated pullback using the stent database. Since y and $\hat{y}$ are required to have equal sizes for error calculation, y was defined to have a constant size regardless of the number of points in generated pullback, as described in section 7.6.

To test the feasibility and accuracy of the method, a pullback generated with known parameters was assumed as y and initial parameters that were close to the actual parameters was specified to start the Levenberg-Marquardt algorithm. One of the challenges of

optimization using this objective function, is the relatively large errors when parameters are far from the solution and a small change in parameters (Δp) used to find the Jacobian matrix does not make a necessary change in the calculated error and so the algorithm fails to converge. As a result, minimum Δp was increased from 10^{-6} to 10^{-2} and the tolerance was increased from 10^{-6} to 10^{-4}.

Case 1: A pullback generated using parameter values: x_c = 0.1 mm, y_c = 0.1 mm, z_p = 0 mm, φ_p = 0 rad, φ_c = 0 rad, and θ_c = 0.25 rad was considered as data y_1 and initial parameters (in the above order) was specified p_o = [0.05, 0.05, 0, 0, 0, 0.20]. Using λ=0.01 (the default value), algorithm converged after 24 iterations (calling objective function 329 times). Returned parameters were $p_{solution}$ = [0.9999, 0.1000, 0, -0.0008, 0.007, 0.2500] with χ^2 = 13.80.

Case 2: Data y_1 defined in case 1 was considered with initial parameters further from actual values, p_o = [0, 0, 0, 0, 0, 0]. Algorithm converged after 112 iterations (calling objective function 1482 times). Returned parameters were $p_{solution}$ = [0.1, 0.1, 0, 0, 0, 0.26] with χ^2 = 1043.39.

Error analysis

The calculated χ^2 includes two types of errors: 1) a mismatch between simulated (y) and fitted ($\hat{y}|_p$) IVOCT pullbacks corresponding to when an A-scan in the simulated does not match the fitted or vice versa; and 2) A-scans that do intersect a strut in both simulated and fitted pullbacks, however, neighboring points on the strut deviate. Figure 7.11-a illustrates the error between and over the entire pullback. Number of A-scans with non-zero value of error is 4258 where total number of A-scans is 100,000.

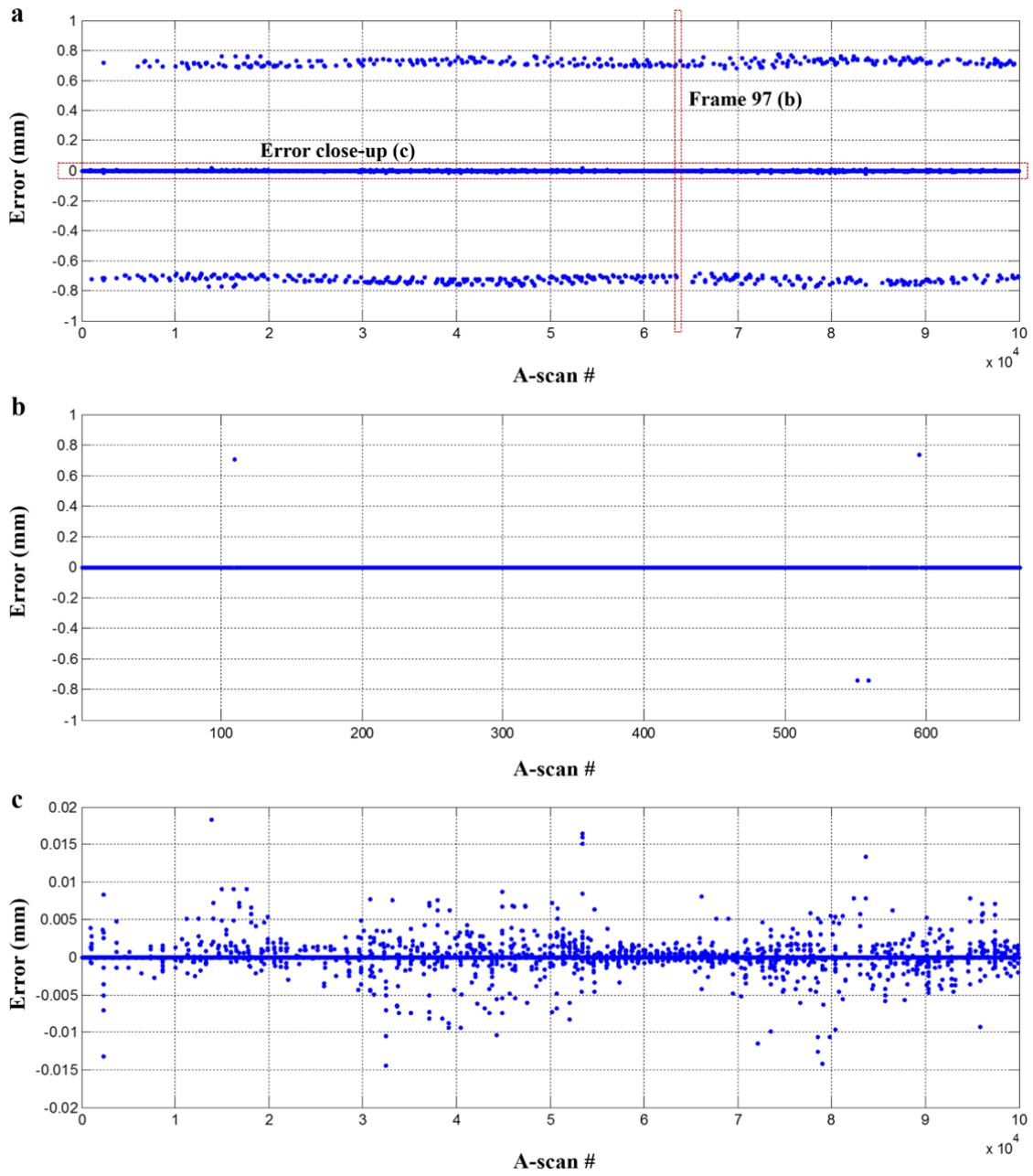

Figure 7.11: a) Error between y and $\hat{y}|_p$ plotted over entire pullback (100,000 A-scans), **b)** selected B-scan (#97), **c)** close-up of error in -20 to 20 µm range.

Errors with an absolute value in range of 0.6 to 0.8 mm corresponds to mismatch of A-scans, giving 2272 data points. Considering each B-scan consists of 666 A-scans,

there are on average 3.5 mismatched A-scans in each B-scan (Figure 7.11-b). The rest of error data indicates deviation between neighboring points on the struts which results in a different depth recorded by A-scans. Figure 7.11-c illustrates a close-up of Figure 7.11-a in range of 2 to 20 μm. Error values are bracketed by 10 μm which is within resolution of IVOCT system.

The test cases demonstrated the practicality of Levenberg-Marquardt algorithm for this optimization problem. A primary source of error between simulated and fitted IVOCT pullback corresponds to unmatched A-scans. Unmatched A-scans correspond to cases when either a strut is present in the simulated data and not present in the fitted data or when a strut is not presence in the simulated data and is in the fitted data. Inasmuch as missed struts are a primary source of error between simulated and fitted data, an alternative error function that accounts for variance in both dimensions (i.e., scan depth and A-scan number) in the IVOCT pullback should be considered. For example, an error function that does not severely penalize adjacent A-scans in simulated and fitted data that have a strut at approximately the same depth may provide improved results.

Chapter 8: Conclusions and discussions

CONCLUSIONS

The objective of my research was to characterize and correct artifacts associated with IVOCT images of coronary stents. IVOCT provides images at resolution of 10-15 um, making this technique a preferred assessment technique in coronary stenting, nevertheless, imaging artifacts have not been thoroughly studied. Clinical use of IVOCT to assess coronary stenting will benefit from the characterization and correction of various artifacts. In my research, two models were created; a physical blood vessel model to acquire images under controlled conditions and a computer model using physical and physiological based parameters to perform optical simulations.

Sunflower effect

The sunflower effect is observed when imaging metal coronary stents and appears as a bending of stent struts toward IVOCT catheter. Sunflower effect occurs when the catheter is at eccentric positions in the vessel lumen. Results of this work suggests when an eccentric IVOCT catheter emits light that is incident on a metal stent strut at any angle, returning light to the catheter is reflected from a small-sized region on the metal strut surface. The regions that reflect light back into the catheter have a surface normal that is oriented along the light direction. As light transmits from the catheter, a finite beam width at the stent strut ensures return reflections are recorded at each angular position. Since reflections return from a small-sized region on the stent strut, echo-time is nearly constant at each angular position and the metal strut appears in IVOCT images as a straight line bending towards the catheter.

Malapposition measurement

Inasmuch as IVOCT stent measurements are at an early stage, no comprehensive consensus methodology exists on how to measure stent malapposition that is uniformly agreed upon. Results of this study confirms the accuracy of one the methods used in clinical practice in which the user draws a line-segment from center of the strut blooming in the IVOCT image to the luminal wall that indicates the shortest distance, malapposition is determined by subtracting the known strut thickness from the measured distance. Observation of all stent struts in the IVOCT image is proposed where a circle is drawn tracing the circumference of the stent and lines are drawn from the center of strut blooming to the arterial wall perpendicular to the circle and the measured malapposition distances match the actual values.

Evaluation of IVOCT in neointima thickness measurement

Measurements of neonitimal thickness from IVOCT images were compared to values obtained from Micro-CT images which represent actual neointimal thickness. We were able to measure the thickness of neointimal layers in IVOCT images as thin as 30 μm accurately in presence of 5% blood. Fractional error in IVOCT measurements of thin and thick neointima was 0.03 and 0.27, respectively. User placement of a line segment results in larger errors when measuring thin neointimas, nonetheless an error of 10 μm is within the resolution of IVOCT.

Effect of thick neointimas

Optical simulations validate the mechanism of the merry-go-round effect in presence of thick neointima; as the neointimal layer becomes thicker, reflections from the strut surface undergo multiple scattering events and are collected by the IVOCT catheter. Therefore, struts in the IVOCT image appear elongated and the arterial wall is observed

behind the artifactually formed edges while shadowing is confined to the mid portion of the strut. Similarly, when the catheter is at eccentric positions, multiple scattering events inside neointima results in recording reflections from more regions on the strut while the initial direction of reflections deviate from a specularly reflected incoming beam. Consequently, sunflower effect is not pronounced.

Bioabsorbable stents

Surface reflections of bioabsorbable and metallic stents were investigated. Specular reflection was the primary source of reflection in Cypher stent, resulting in strong reflections that are dependent on the direction of incident beam. In case of Absorb stent, directional diffuse is of the same order of magnitude compared to specular values, causing the incident beam to backscatter to the catheter regardless of the incident light direction. Consequently, reflections from the entire strut surface are observed and struts appear as empty boxes due to homogeneity of the polymer. Furthermore, Micro-CT images illustrated the bright spots inside struts corresponds to hollow spaces between the struts when they separate or merge together and do not necessarily indicate presence of micro fractures. Finally, Micro-CT images also suggest that shape of struts in IVOCT images can be artifactually deformed from the true shape.

Artifact correction algorithm

An algorithm was developed which replaces the apparent stent struts in IVOCT pullback images with the actual stent structure obtained by Micro-CT imaging. Simulated pullback was generated using a stent database and catheter position and orientation. Levenberg-Marquardt algorithm was ulitized to fit the simulated pullback to the actual IVOCT pullback data, by finding values of desired transformation parameters. Feasibility

and accuracy of this method was tested using a pullback generated with known parameters as IVOCT pullback data.

FUTURE STUDIES

Applying correction algorithm to IVOCT pullback

Having shown the practicality of Levenberg-Marquardt algorithm by using simulated pullback as input data, the next step is using IVOCT pullback of phantom vessels where catheter position and orientation is controlled. Pullbacks need to be modified to match the defined y data type by segmenting the struts and assigning the depth to the A-scans and assigning zero to A-scans with no strut. The presence of a guide wire, however, will complicate the optimization as it casts a shadow for each revolution and the corresponding A-scans do not convey any information about stent reflection.

Using pullback data to initialize catheter parameters

Catheter position and orientation can be estimated from IVOCT images and specified as initial values. Catheter position with respect to arterial wall is located since it is at the center of IVOCT images. Average of catheter position over few frames provides initial values of x_c and y_c. Change in catheter position over the entire pullback can provide an estimate of φ_c and θ_c. Defining initial values of parameters will decrease computation time and improve the value of χ^2.

Incorporating vessel tortuosity and luminal area variation

The simulated pullback at present is generated assuming stent is deployed in a straight vessel with constant luminal area and therefore can be applied only IVOCT pullbacks of phantom vessels. Coronary arteries are tortuous and luminal area varies along

the stented length of the artery, especially in presence of atherosclerotic plaques. Simulated pullback will be modified to include bends and variation in cross sectional area.

References

1. "Heart disease and stroke statistics-2012 update: A report from the American heart association" Circulation. **125**, 2-220 (2012).
2. G. K. Hansson, "Inflammation, Atherosclerosis, and Coronary Artery Disease" N. Engl. J. Med. **352**, 1685-1695 (2005)
3. http://www.healthsym.com/reverse-and-aortic-atherosclerosis.html
4. http://www.mayoclinic.com/health/coronary-artery disease/
5. http://www.ptca.org/pr_gen/19940803_fda.html
6. G. Dangas, F. Kuepper, "Restenosis: Repeat Narrowing of a Coronary Artery Prevention and Treatment" Circulation. **105,** 2586-2587(2002).
7. http://www.fda.gov/NewsEvents/Newsroom/PressAnnouncements/2008/ucm116848.htm
8. http://bmctoday.net/citoday/2009/07/article.asp?f=CIT0709_07.php
9. http://www.kyoto-mp.co.jp/news/080125_en.html
10. N. J. Wimmer and R. W. Yeh, "Another View of Personalized Medicine: Optimizing Stent Selection on the Basis of Predicted Benefit in Percutaneous Coronary Intervention" Trends Cardiovas. Med. **22**, 23-28 (2012).
11. D. Huang, E. A. Swanson, C. P. Lin, J. S. Schuman, W. G. Stinson, W. Chang, M. R. Hee, T. Flotte, K. Gregory, C. A. Puliafito, J. G. Fujimoto, "Optical coherence tomography", Science **254**, 1178–1181 (1991).
12. J. G. Fujimoto, "Optical coherence tomography" C. R. Acad. Sci. IV Phys. **2**, 1099-1111 (2001).

13. http://www.uhhospitals.org/services/heart-and-vascular/institute/centers/cardiovascular-imaging/cardiovascular-imaging-core-laboratory/services/optical-coherence-tomography#prettyPhoto
14. G. N. Levine, J. C. Blankenship, S. R. Bailey, J. A. Bittl, B. Cercek, C. E. Chambers, S. G. Ellis, R. A. Guyton, S. M. Hollenberg, U. N. Khot, R. A. Lange, L. Mauri, R. Mehran, I. D. Moussa, D. Mukherjee, B. K. Nallamothu, H. H. Ting, "2011 ACCF/AHA/SCAI Guideline for Percutaneous Coronary Intervention: A Report of the American College of Cardiology Foundation/American Heart Association Task Force on Practice Guidelines and the Society for Cardiovascular Angiography and Interventions" J. Am. Coll. Cardiol. **58**, e44-122 (2011).
15. http://www.ptca.org/ivus/ivus.html
16. J. W. Moses, G. Dangas, R. Mehran, G. S. Mintz, "Drug-Eluting Stents in the Real World: How Intravascular Ultrasound Can Improve Clinical Outcome" Am. J. Cardiol. **102**, 24J–28J (2008).
17. C. Briguori, A. Anzuini, F. Airoldi, G.Gimelli, T. Nishida, M. Adamian, N. Corvaja, C. D. Mario, A. Colombo, "Intravascular Ultrasound Criteria for the Assessment of the Functional Significance of Intermediate Coronary Artery Stenoses and Comparison with Fractional Flow Reserve" Am. J. Cardiol. **87**, 136-141 (2001).
18. A. Fassa, K. Wagatsuma, S. T. Higano, V. Mathew, G. W. Barsness, R. J. Lennon, D. R. Holmes, A. Lerman, "Intravascular Ultrasound-Guided Treatment for Angiographically Indeterminate Left Main Coronary Artery disease: A Long-Term Follow-Up Study" J. Am. Coll. Cardiol. **45**, 204-211 (2005).
19. M. E. Brezinski, G. J. Tearney, B. E. Bouma, J. A. Izatt, M. R. Hee, E. A. Swanson, J. F. Southern, J. G. Fujimoto, "Optical Coherence Tomography for Optical Biopsy:

Properties and Demonstration of Vascular Pathology" Circulation. **93**, 1206-1213 (1996).

20. J. G. Fujimoto, S. A. Boppart, G. J. Tearney, B. E. Bouma, C. Pitris, M. E. Brezinski, "High resolution in vivo intra-arterial imaging with optical coherence tomography" Heart. **82**, 128-133 (1999).
21. J. W. Villard, K. K. Cheruku and M. D. Feldman, "Applications of optical coherence tomography in cardiovascular medicine, part I" J. Nucl. Cardiol. **16**, 287-303 (2009).
22. T. Kubo, T. Imanishi, H. Kitabata, A. Kuroi, S. Ueno, T. Yamano, T. Tanimoto, Y. Matsuo, T. Masho, Sh. Takarada, A. Tanaka, N. Nakamura, M. Mizukoshi, Y. Tomobuchi, T. Akasaka, "Comparison of Vascular Response After Sirolimus-Eluting Stent Implantation Between Patients With Unstable and Stable Angina Pectoris" J. Am. Coll. Cardiol. Img. **1**, 475-484 (2008).
23. M. E. Brezinski, G. J. Tearney, N. J. Weissman, S. A. Boppart, B. E. Bouma, M. R. Hee, A. E. Weyman, E. A. Swanson, J. F. Southern, J. G. Fujimoto, "Assessing atherosclerotic plaque morphology: comparison of optical coherence tomography and high frequency intravascular ultrasound" Heart. **77**, 397-403 (1997).
24. M. Brezinski, M. Brezinski, X. Li, H. Gold, N. Weissman, C. Pitris, K. Saunders, R. Ghanti, and J. Fujimoto, "In vivo intravascular imaging with OCT comparison with ultrasound," in Biomedical Optical Spectroscopy and Diagnostics, T. Li, ed., Vol. 38 of OSA Trends in Optics and Photonics (Optical Society of America, 2000).
25. D. Matsumoto, J. Shite, T. Shinke, H. Otake, Y. Tanino, D. Ogasawara, T. Sawada, O. L. Paredes, K. Hirata, and M. Yokoyama, "Neointimal coverage of sirolimus-eluting stents at 6-month follow-up: evaluated by optical coherence tomography" Eur. Heart. J. **28,** 961-967 (2007).

26. H. G. Bezerra, M. A. Costa, G. Guagliumi, A. M. Rollins, D. I. Simon "Intracoronary Optical Coherence Tomography: A Comprehensive Review" J. Am. Coll. Cardiol. Intv. **2**, 1035-1046 (2009).
27. D. B. Wolfe, R. S. Conroy, P. Garstecki, B. T. Mayers, M. A. Fischbach, K. E. Paul, M. Prentiss, and G. M. Whitesides, "Dynamic control of liquid-core liquid-cladding optical waveguides" PANS, **101 (34)**, 12434-12438 (2004).
28. D. K. Cai, A. Neyer, R. Kuckuk, H.M. Heise, "Optical absorption in transparent PDMS materials applied for multimode waveguides fabrication" Opt. Mater. 30, 1157-1161 (2008).
29. M. Firbank and D. T. Delpy, "A design for a stable and reproducible phantom for use in near infra-red imaging and spectroscopy" *Phys. Med. Biol.* **38,** 847-853 (1993).
30. W. Cheong, S. A. Prahl, and A. J. Welch, "A Review of the Optical Properties of Biological Tissues" IEEE J. Quantum. Elect. **12,** 2166 - 2185 (1990).
31. R. V. Kuranov, A. B. McElroy, N. Kemp, S. Baranov, J. Taber, M. D. Feldman, T. E. Milner, "Gas-Cell Referenced Swept Source Phase Sensitive Optical Coherence Tomography" IEEE Photon. Technol. Lett. **22**, 1524-1526 (2010).
32. W. V. Sorin, D. F. Gray, "Simultaneous Thickness and Group Index Measurement Using Optical Low-Coherence Reflectometry" IEEE Photon. Technol. Lett. **4**, 105-107 (1992).
33. G. J. Tearney, M. E. Brezinski and J. F. Southern, B. E. Bouma, M. R. Hee, and J. G. Fujimoto, "Determination of the refractive index of highly scattering human tissue by optical coherence tomography" Opt. Lett. **20**, 2258-2260 (1995).

34. X. Wang, T. E. Milner, M. C. Chang, J. S. Nelson, "Group refractive index measurement of dry and hydrated type I collagen films using optical low-coherence reflectometry" J. Biomed. Opt. **1**, 212-216 (1996).
35. http://www.photonics.byu.edu/FiberOpticConnectors.parts/images/smf28.pdf
36. S. L. Jacques, C.A. Alter and S.A. Prahl, "Angular dependence of HeNe laser light scattering by human dermis" Lasers. Life. Sci. **1,** 309-334 (1987)
37. M. Friebel, J. Helfmann, U. Netz, M. Meinke, "Influence of oxygen saturation on the optical scattering properties of human red blood cells in the spectral range 250 to 2000 nm," J. Biomed. Opt. **14(3)**, 034001 (2009).
38. Zemax® 12 User's Manual, Radiant Zemax, LLC, Redmond, WA.
39. D. Marcuse, "Loss analysis of single-mode fiber splices" The Bell System Technical Journal **56 (5)**, (1977).
40. G. J. Tearney, E. Regar, T. Akasaka, et al, "Consensus standards for acquisition, measurement, and reporting of intravascular optical coherence tomography studies: a report from the international working group for intravascular optical coherence tomography standardization and validation," J. Am. Coll. Cardiol. **59**, 1058-1072 (2012).
41. Discussion with J. Dijkstra, Ph.D., Leiden university medical center, The Netherlands.
42. G. J. Ughi, T. Adriaenssens, K. Onsea, P. Kayaert, C. Dubois, P. Sinnaeve, M. Coosemans, W. Desmet, J. D'hooge, "Automatic segmentation of in-vivo intra-coronary optical coherence tomography images to assess stent strut apposition and coverage," Int. J. Cardiovasc. Imag. **28,** 229-224 (2011).

43. M. Joner, A.V. Finn, A. Farb, E.K. Mont, F.D. Kolodgie, E. Ladich, R. Kutys, K. Skorija, H.K. Gold, R.Virmani, "Pathology of drug-eluting stents in humans: delayed healing and late thrombotic risk" J. Am. Coll. Cardiol. **48**, 193-202 (2006).
44. A. V. Finn, M. Joner, G. Nakazawa, F. Kolodgie, J. Newell, M. C. John, H. K. Gold, R. Virmani, "Pathological Correlates of Late Drug-Eluting Stent Thrombosis Strut: Coverage as a Marker of Endothelialization" Circulation. **115**, 2435-2441 (2007).
45. A. Murata, A. Murata, D. Wallace-Bradley, A. Tellez, C. Alviar, M. Aboodi, A. Sheehy, L. Coleman, L. Perkins, G. Nakazawa, G. Mintz, G.L. Kaluza, R. Virmani, J.F. Granada, "Accuracy of optical coherence tomography in the evaluation of neointimal coverage after stent implantation" J. Am. Coll. Cardiol. Img. **3**, 76-84 (2010).
46. G. Nakazawa, A. V. Finn, M. Joner, E. Ladich, R. Kutys, E. K. Mont, H. K. Gold, A. P. Burke, F. D. Kolodgie, R. Virmani, "Delayed Arterial Healing and Increased Late Stent Thrombosis at Culprit Sites After Drug-Eluting Stent Placement for Acute Myocardial Infarction Patients: An Autopsy Study" Circulation. **118**, 1138-1145 (2008).
47. P. G. Anderson, R. K. Bajaj, W. A. Baxley, G. S. Roubin, "Vascular pathology of balloon-expandable flexible coil stents in humans" J. Am. Coll. Cardiol. **19**,272-381 (1992).
48. R. Komatsu, M. Ueda, T. Naruko, A. Kolima, S. E. Becker, "Neointimal tissue response at sites of coronary stenting in humans: macroscopic, histological, and immunohistochemical analysis" Circulation. **98**, 224-233 (1998).
49. H. M. M. Van Beusekom, W. J. Van der Geissen, R. J. Van Suylen, E. Bos, F. T. Bosman, P. W. Serruys, "Histology after stenting of human saphenous vein bypass

grafts: observations from surgically excised grafts 3 to 320 days after stent implantation" J. Am. Coll. Cardiol. **21**, 45–54 (1993).

50. A. Farb, G. Sangiorgi, A. J. Carter, V. M. Walley, W. D. Edwards, R. S. Schwartz, R. Virmani, "Pathology of Acute and Chronic Coronary Stenting in Humans" Circulation. **99**, 44-52 (1999).
51. E. Salomatina, B. Jiang, J. Novak, A. N. Yaroslavsky, "Optical properties of normal and cancerous human skin in the visible and near-infrared spectral range" J. Biomed. Opt. **11**, 064026 (2006).
52. H. Ding, J. Q. Lu, W. A. Wooden, P. J. Kragel and X. Hu, "Refractive indices of human skin tissues at eight wavelengths and estimated dispersion relations between 300 and 1600 nm" Phys. Med. Biol. **51**,1479-1489 (2006).
53. J. A. Ormiston, P. W.S. Serruys, "Bioabsorbable Coronary Stents" Circ. Cardiovasc. Interv. 2, 255-260 (2009).
54. J. A. Ormiston, P. W Serruys, E. Regar, D. Dudek, L. Thuesen, M. W. I. Webster, Y. Onuma, H. M Garcia-Garcia, R. McGreevy, S. Veldhof, "A bioabsorbable everolimus-eluting coronary stent system for patients with single de-novo coronary artery lesions (ABSORB): a prospective open-label trial" Lancet. **371**, 899-907(2008).
55. R. Waksman, "The BIOTRONIK Bioabsorbable Magnesium Scaffold DREAMS" Angioplasty summit TCTAP (2011)
56. J. W. Currier, D. P. Faxon. "Restenosis after percutaneous transluminal coronary angioplasty: have we been aiming at the wrong target?" J. Am. Coll. Cardiol. **25**, 516-520 (1995).
57. G. S. Minz, J. J. Popma, A. D. Pichard, "Arterial remodeling after coronary angioplasty: a serial intravascular ultrasound study" Circulation. **94,** 35-43 (1996).

58. A. J. Lansky, G. S. Mintz, J. J. Pompa JJ, "Remodeling after directional coronary atherectomy (with and without adjunct percutaneous transluminal coronary angioplasty): a serial angiographic and intravascular ultrasound analysis from the Optimal Atherectomy Restenosis Study. J. Am. Coll. Cardiol. **32,** 329-337 (1998).
59. H. Tamai, K. Igaki E. Kyo, K. Kosuga, A. Kawashima, S. Matsui, H. Komori, T. Tsuji, S. Motohara, H. Uehata, "Initial and 6-Month Results of Biodegradable Poly-*l*-Lactic Acid Coronary Stents in Humans" Circulation.**102,** 399-404 (2000).
60. R. Erbel, C. Mario, J. Bartunek, J. Bonnier, B. Bruyne, F. R Eberli, P. Erne, M. Haude, B. Heublein, M. Horrigan, C. Ilsley, D. Böse, J. Koolen, T. F Lüscher, N. Weissman, R. Waksman, "Temporary scaffolding of coronary arteries with bioabsorbable magnesium stents: a prospective, non-randomised multicentre trial" Lancet, **369(9576),** 1869-1875 (2007).
61. M. Haude, R. Erbel, P. Erne, S. Verheye, P. Vermeersch, H. Degen, R. Waksman, N. Weissman, F. Prati, J. Koolen, "Six and Twelve-month Clinical and Imaging Results of the Multicenter First-in-man BIOSOLVE-I Study with the Paclitaxel-Eluting Bioabsorbable Magnesium Scaffold (DREAMS)" AHA meeting, Circulation, 126, **A10029 (2012).**
62. X. D. He, K. E. Torrance, F. X. Sillion, D. P. Greenberg, "A comprehensive physical model for light reflection" Comp. Graph. (SIGGRAPH '91 Proceedings), **25(4),** 175-86, (1991).
63. G. Binnig, C. F. Quate, C. Gerber, "Atomic Force Microscope" Phys. Rev. Lett. **56**, 930-933 (1986)
64. G. Meyer and N. M. Amer, "Novel optical approach to atomic force microscopy", Appl. Phys. Lett. **53**, 1045-1047 (1988).

65. C. Y. Poon, B. Bhushan, "Comparison of surface roughness measurements by stylus profiler, AFM and non-contact optical profiler" Wear, **190**, 76-88 (1995).
66. http://www.asylumresearch.com/Applications/CombinedAFMOptical/CombinedAFMOptical.shtml
67. http://www.nanosensors.com/PPP-FMR.htm
68. B. Karlsson and C. G. Ribbing, "Optical constants and spectral selectivity of stainless steel and its oxides" J. Appl. Phys. **53**, 6340 (1982).
69. Francis Esmonde-White, University of Michigan, May 2010. http://www.esmonde-white.com/home/diversions/matlab-program-for-loading-stl-files
70. http://zone.ni.com/reference/en-XX/help/371361J-01/gmath/3d_cartesian_coordinate_rotation_euler/
71. H. Gavin, "The Levenberg-Marquardt method for nonlinear least squares curve-fitting problems", Department of Civil and Environmental Engineering, Duke University, September 28, 2011
72. M. I. A. Lourakis, "Brief Description of the Levenberg-Marquardt Algorithm Implemened by levmar", Institute of Computer Science, Foundation for Research and Technology - Hellas, February 11, 2005
73. D.W. Marquardt, "An algorithm for least-squares estimation of nonlinear parameters" J. Soc. Indust. Appl. Math. **11(2),** 431-441 (1963)
74. K. Madsen, N. B. Nielsen, and O. Tingleff. "Methods for nonlinear least squares problems", Technical Report. Informatics and mathematical modeling, Technical University of Denmark, 2004.
75. MATLAB help